Laboratori Nazionali di Frascati

LNF-69/2

W. Ash, D. Grossman, G. Matthiae, G. P. Murtas, M. Nigro, G. K. O'Neill, G. Sacerdoti, R. Santangelo, D. Scannicchio, and E. Schiavuta : A MAGNETIC ANALYZER TO BE USED FOR ADONE COLLIDING BEAM EXPERIMENTS.

Laboratori Nazionali di Frascati del CNEN
Servizio Documentazione

LNF-69/2

Nota Interna: n. 425
7 Gennaio 1969

W. Ash(x), D. Grossman(x), G. Matthiae(+), G. P. Murtas, M. Nigro(x), G. K. O'Neill(x), G. Sacerdoti, R. Santangelo(x), D. Scannicchio(o) and E. Schiavuta(x): A MAGNETIC ANALYZER TO BE USED FOR ADONE COLLIDING BEAM EXPERIMENTS. -

I. - INTRODUCTION. -

The detection apparatus described in this report was designed to completely analyze the particles produced in e^+e^- collisions in Adone at energies between .75 and 3.0 GeV.

This apparatus is particularly suited for:

- momentum and direction measurements of charged particles;
- γ-ray detection with localization of the materialization point;
- range measurements and detection of nuclear and electromagnetic interactions.

Its main parts are a large cylindrical coil which produces a 4.5 kG magnetic field in its interior and a spark chamber system placed inside and outside of the coil. The internal spark chambers with thin electrodes measure the initial direction and the momentum of the charged particles. In the external thick plate chambers the γ-rays convert and the charged particles are further analyzed (range measurements, nuclear and electromagnetic interactions etc.).

Essentially we have adopted the solutic proposed by a previous study Commitee(1) i.e. a solenoid which can be mounted with its axis parallel to the Adone straight section (longitudinal arrangement) or perpendicular to it (transverse arrangement). As the details of the project were worked out, certain modifications were made on this preliminary design, the most important of which was the addition of a compensation system for the transverse case. In this report we discuss only the transverse arrangement in detail, treating in the Appendix those features in which the longitudinal case differs.

Although it appears that the transverse arrangement is in any case the most feasible (especially from the stand point of construction), nevertheless it seems advisable to maintain a longitudinal alternative as far as possible in view of the much smaller problems of magnet-

---

(x) - Princeton University
(+) - Istituto Superiore di Sanità, Roma
(x) - INFN, Sezione di Padova
(o) - INFN, Gruppo di Pavia.

-beam interactions involved in the latter.

Before continuing the description of the apparatus, it is convenient to introduce now some geometrical definitions.

Let (x, y, z) be the cartesian reference system with its origin in the center of e^+e^- interaction region, oriented as in Fig. 1, $\vec{u}$ an unit vector along a straight line passing through

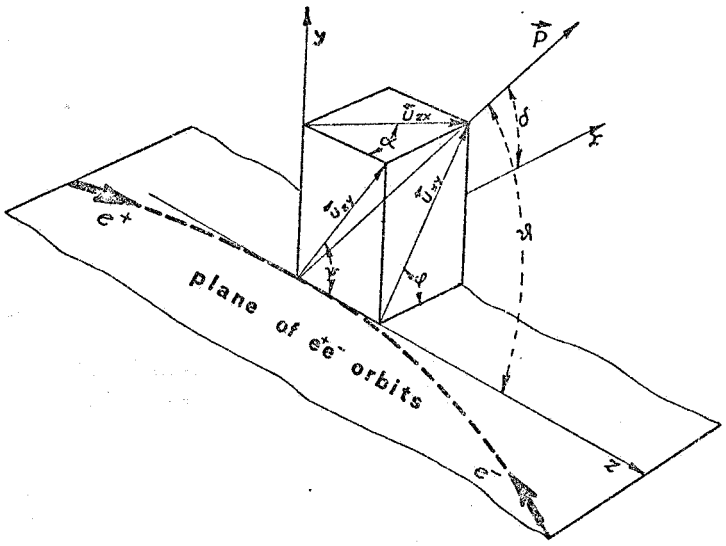

FIG. 1 - Definition of the cartesian and angular coordinate systems. The dotted line represents the beam trajectories in Adone. The angles (θ, φ) and (δ, ψ) form two pairs of polar angular coordinates with polar axis along z and x respectively.

the origin; u_x, u_y, u_z its cartesian components; $\vec{u}_{xy}$, $\vec{u}_{xz}$, $\vec{u}_{yz}$ the orthogonal projections of $\vec{u}$ on the planes (xy), (xz), (yz); and at last $\vec{x}$, $\vec{y}$, $\vec{z}$, the vectors of the reference system. We define two polar coordinates (θ, φ) through the relations

$$\cos\theta = \vec{u} \cdot \vec{z} \qquad \cos\varphi = \vec{u}_{xy} \cdot \vec{x} \tag{1}$$

We choose z as the polar axis as it is the axis of cylindrical symmetry in the dynamics of e^+e^- interactions, in the absence of polarization of the beams. Since the detection apparatus has in its essential parts a cylindrical symmetry along the x axis, we introduce a second pair of polar coordinates (δ, ψ) defined by:

$$\cos\delta = \vec{u} \cdot \vec{x} \qquad \cos\psi = \vec{u}_{yz} \cdot \vec{z} \tag{2}$$

For these coordinates x is the polar axis. Finally, to define the areas with vertical edges it is useful to introduce the angle α :

$$\cos\alpha = \vec{u}_{xz} \cdot \vec{z} \tag{3}$$

The geometrical meaning of all the angles defined above is shown in Fig. 1. The connection between α, δ, ψ and the angles θ, φ are

$$\begin{aligned} \cos\delta &= \sin\theta \cos\varphi \\ \operatorname{tg}\psi &= \sin\varphi \operatorname{tg}\theta \\ \operatorname{tg}\alpha &= \cos\varphi \operatorname{tg}\theta = (\operatorname{tg}\delta \cos\psi)^{-1} \end{aligned} \tag{4}$$

The relations between the cartesian component u_x, u_y, u_z and the two sets of polar coordinates are:

$$\begin{aligned} u_x &= \sin\theta \cos\varphi = \cos\delta \\ u_y &= \sin\theta \sin\varphi = \sin\delta \sin\psi \\ u_z &= \cos\theta = \sin\delta \cos\psi \end{aligned} \tag{5}$$

In Fig. 2 are shown the principal kinds of surface with which we will have to deal in the following.

The next paragraph in which we give a general description of the apparatus is followed by paragraphs dealing in detail with particular arguments such as magnetic interferences with Adone (§ III), acceptances (§ IV) and accuracy (§ V, VI, VII) of the detection system, external spark chamber use (§ VIII), monitor systems (§ IX), gas control system for spark chambers (§ X).

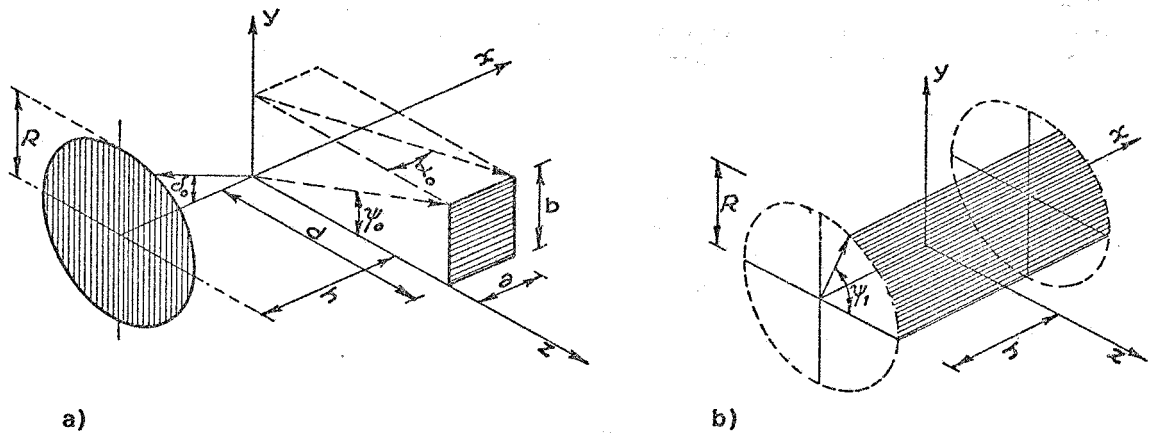

FIG. 2 - Angular definition of various areas of the apparatus. $\alpha \leq \alpha_0$, $\psi \leq \psi_0$ Fig. 2a rectangular area (compensator); $\delta \leq \delta_0$ Fig. 2a circular area (plane wire spark chamber C3); $\delta \leq \delta_0$, $\psi \leq \psi_0$ Fig. 2b cylindrical sector (spark chamber C1, C2)

II. - DESCRIPTION OF THE APPARATUS. -

The apparatus shown in Fig. 3 in a schematic form, consists of the following parts:

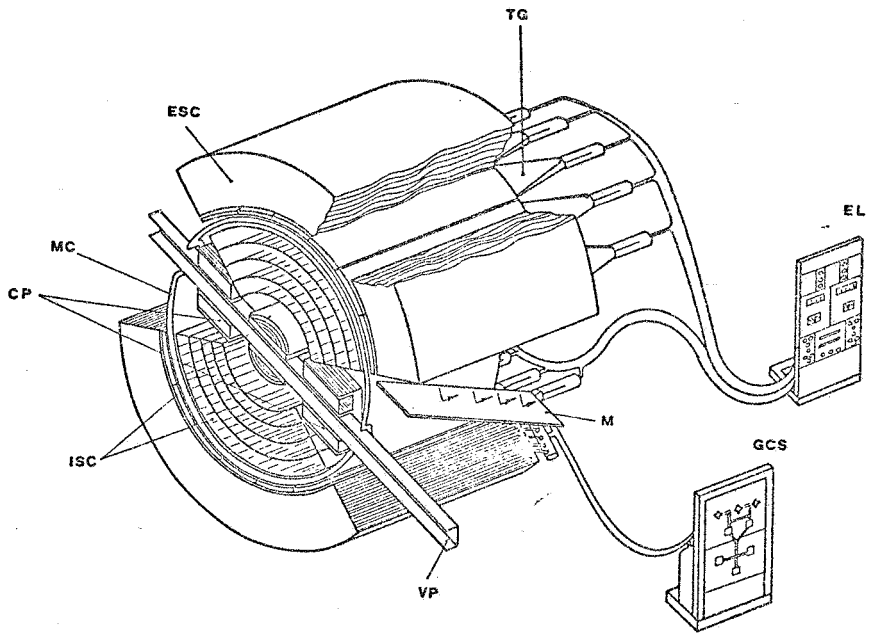

FIG. 3 - Schematic drawing of the magnetic system and of the detection apparatus; MC = main coil; CP = compensators; VP = vacuum pipe; ISC and ESC = internal and external spark chambers; TG = trigger counters; EL = electronic logic; M = mirror; GCS = gas control system.

a) the magnetic system composed of the main coil (MC) and the compensators (CP)[2];
b) a spark chamber system external to the main coil with thick plates (ESC);
c) a spark chamber system internal to the main coil (ISC) for momentum analysis in the magnetic field;
d) the scintillation counters used in forming the spark chamber trigger (TG);
e) the optics;
f) a monitor system for luminosity measurements in Adone;
g) the electronic logic (EL);
h) a gas control system for the spark chambers (GCS);
i) the straight section of the Adone vacuum pipe (VP);
l) the support frame.

a) - Magnetic System. -

This consists of a main cylindrical coil with its axis perpendicular to the straight section of Adone, in which a magnetic field B of about 4.5 kG is maintained, and of two compensator magnets placed in the position shown schematically in Fig. 3. The main features of the coil and of the compensators are summarized in Table 1, 2 and in Fig. 4. In Table 3 are listed the features of the power supply[26].

TABLE 1 - Main Coil

Dimensions: length		200 cm
internal diameter		200 cm
external diameter		214 cm
Magnetic field		4500 gauss
Current		5000 A
Voltage		260 V
Power dissipated		1300 KW
Number of turns		180 wound in 2 overlapping layers
Coil cross section		34 x 21 mm with a 7 mm diameter central hole
Iron cross section (flux return)		4 bars 45 x 45 cm^2
Cooling water	flow rate	about 15 liter/sec
	pressure	10 Atm.
Weight		~ 2000 Kg.

TABLE 2 - Compensator

Dimensions: (see Fig. 4)		
(each) vertical		400 mm
length (max)		740 mm
width		600 mm
Magnetic field at the center		4500 gauss
Power dissipated		300 KW each - 600 KW total
Magnetic field in iron		12 - 18 kG
Cooling water	flow rate	3.5 liter/sec each
	pressure	4 Atm
Weight		350 Kg each

TABLE 3 - Power Supply

Current	5000 A
Voltage	400 V
Stabilization	.1%

FIG. 4a

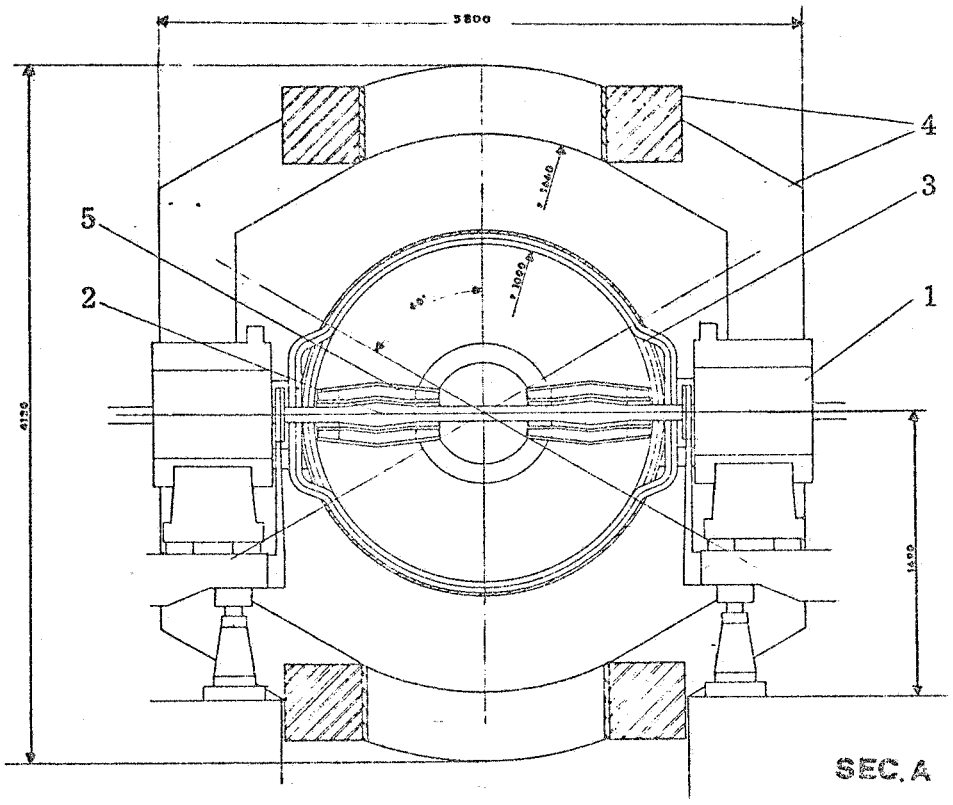

(all dimensions are in mm)

FIG. 4b

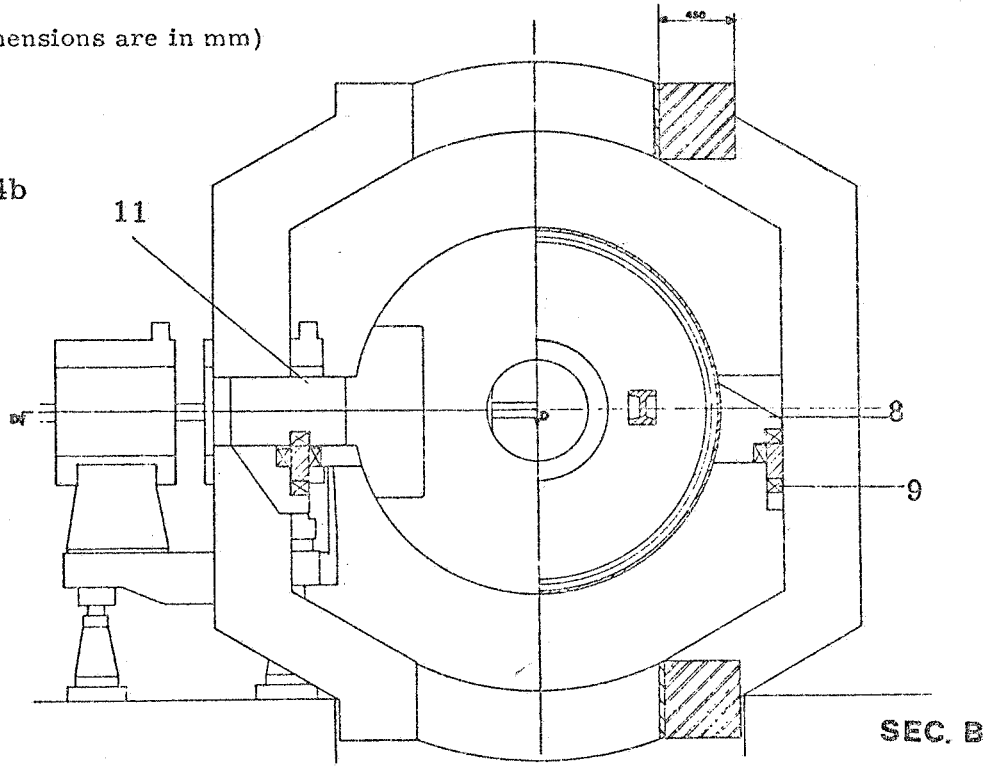

FIG. 4 - Drawings of the magnetic system (solenoid and compensators).
1 = quadrupole; 2 = vacuum pipe straight section; 3 = magnet main coil; 4 = flux return iron; 5 = compensator; 6 = frontal iron plate; 7 = main coil container; 8 = support system; 9 = cooling water pipes and electric connections; 10 = rails for magnet diassembly; 11 = iron for flux return; 12 = support for compensators.

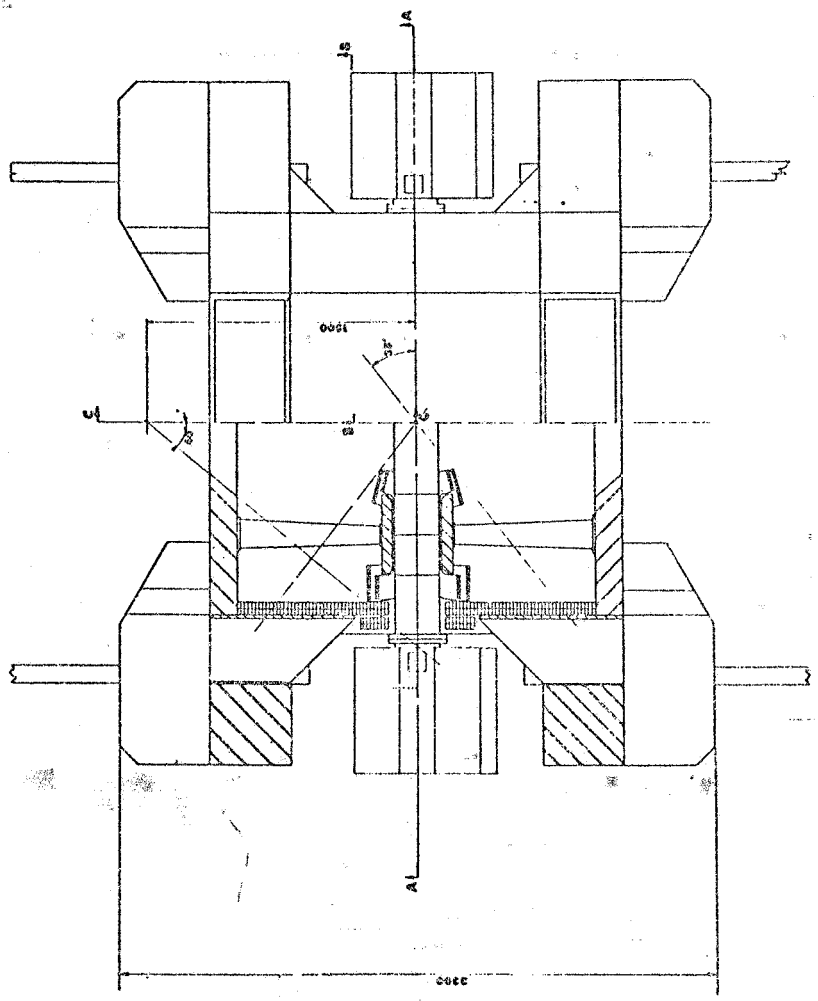

FIG. 4c

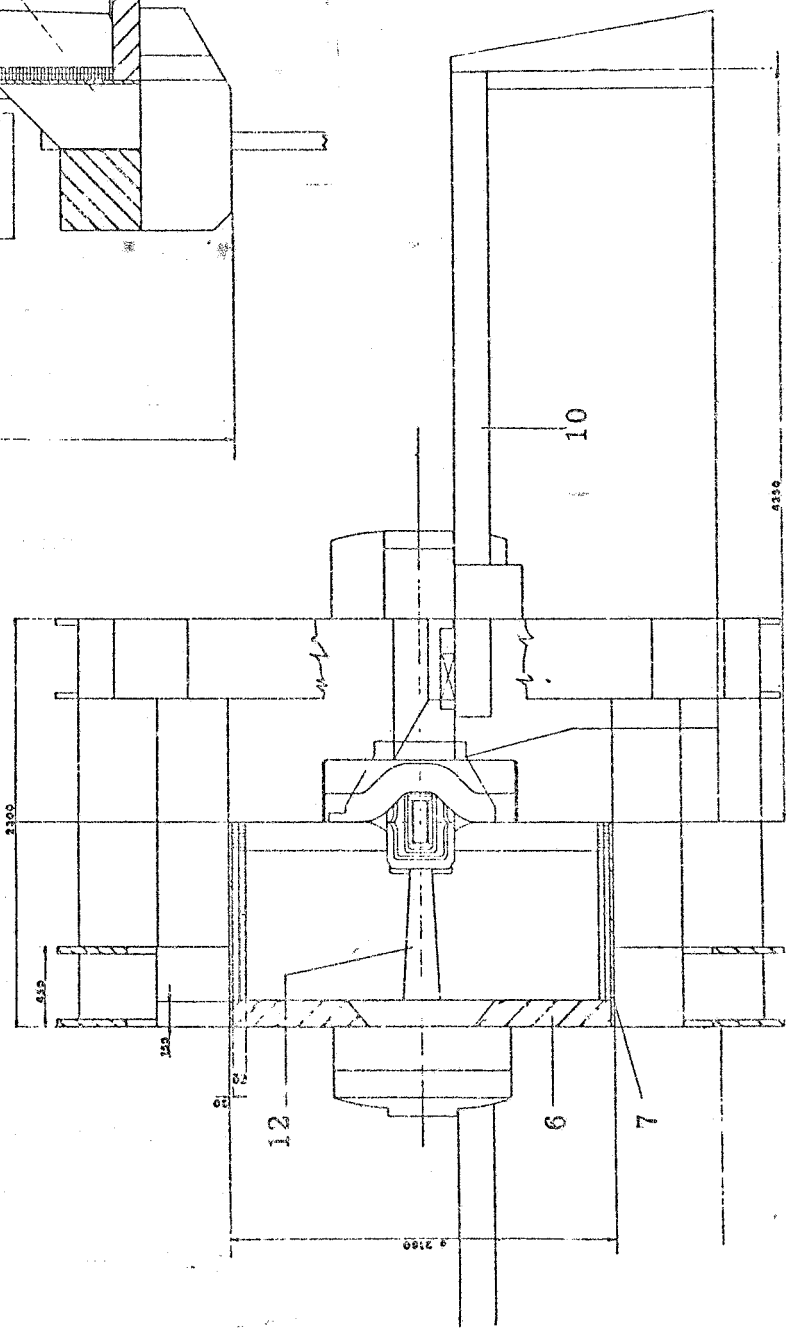

FIG. 4d

SEC.C

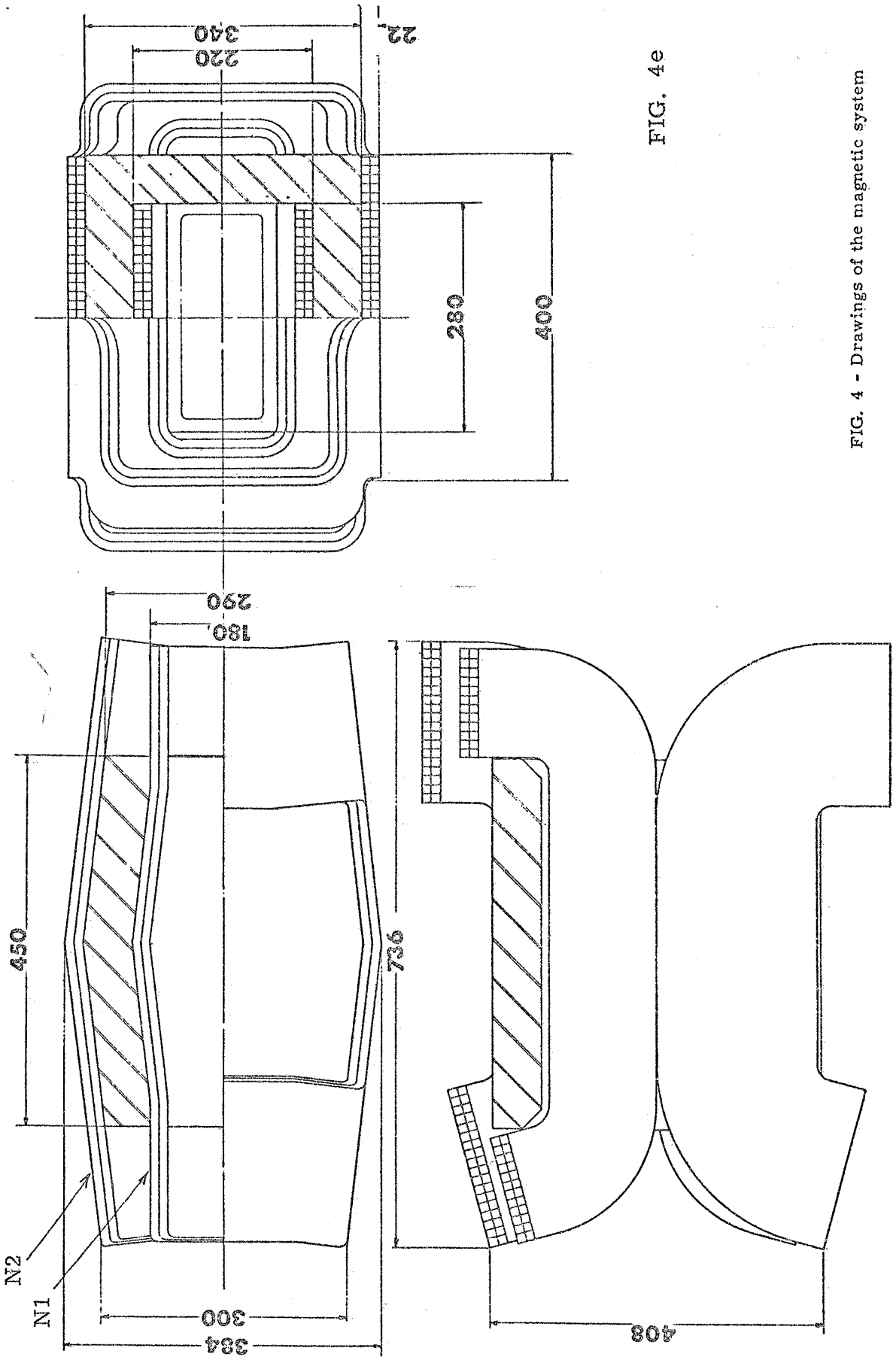

FIG. 4e

FIG. 4 - Drawings of the magnetic system

The magnetic flux is conveyed outside the main coil through two large iron plates placed at the ends of the coil and connected by lateral bars (see Fig. 5).

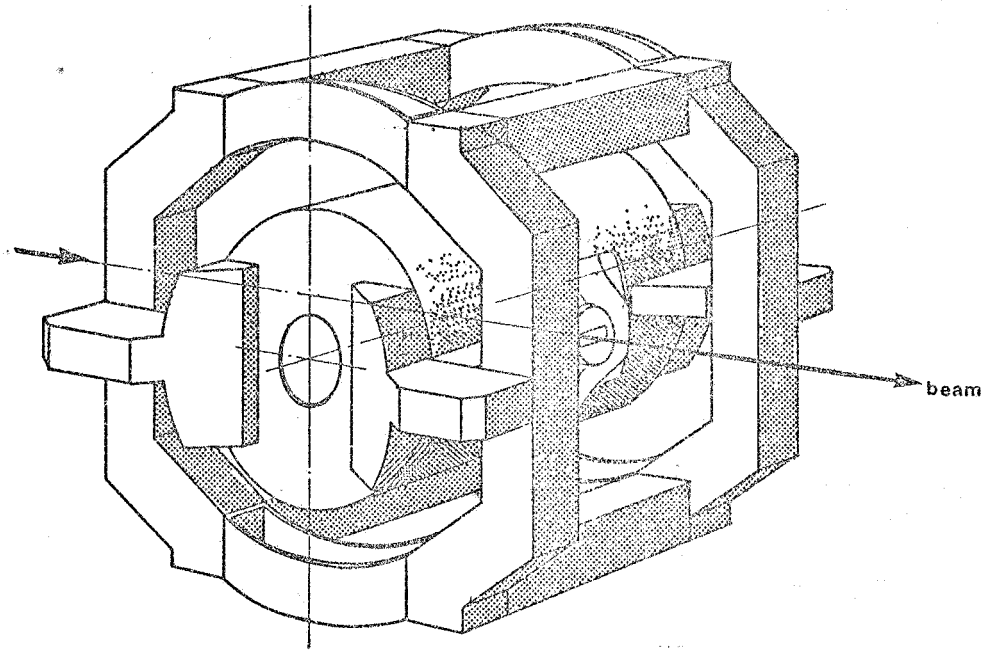

FIG. 5 - Solenoid with the front iron plates connected to the lateral bars for flux return.

The magnetic field within the compensators is uniform, equal in magnitude and opposite in direction to the field of the main coil.

We will discuss later (§ III) the magnetic properties and the functions of the coil+compensator system: at present we only point out that it was designed to make the magnetic interferences with Adone tolerable.

The dimensions of the compensators in angular space are represented by two plane rectangular surfaces perpendicular to the z axis, placed symmetrically with respect to the interaction point with a horizontal aperture of $\alpha_{max} = 38^{o}$ and a vertical one of $\psi_{max} = 33^{o}$ (see Fig. 2a for definitions). Except for this angular region all the internal space of the main coil is available for momentum analysis.

b) - External Spark Chambers (ESC). -

The main coil of the magnet is completely surrounded by ~ 15 cylindrical bigaps spark chambers interleaved with iron plates (see Fig. 6). The radius of curvature of the chambers ranges from 110 cm to 165 cm with length of about 260 cm, and gap height of ~ 1 cm.

The electrodes are made of highly reflecting aluminium plates[3]. As the internal surfaces are specularly reflecting, the spark can be observed tangentially to the cylindrical surface, as well as coaxially. The accuracy in the spark localization on the tangent view is ~ 1 mm. In all other features these spark chambers are not different from those built in other laboratories.

The arrangement of the external spark chambers and their mirrors is shown in Fig. 7 and 10b. The photographs are taken by two cameras placed at both ends of the solenoid.

It is possible to replace some bigaps with scintillation counters in order to trigger the spark chambers only or also on photons converted in the iron or in the main coil.

This apparatus allows: γ detection, e, π, μ discrimination, and range analysis of medium energy particles.

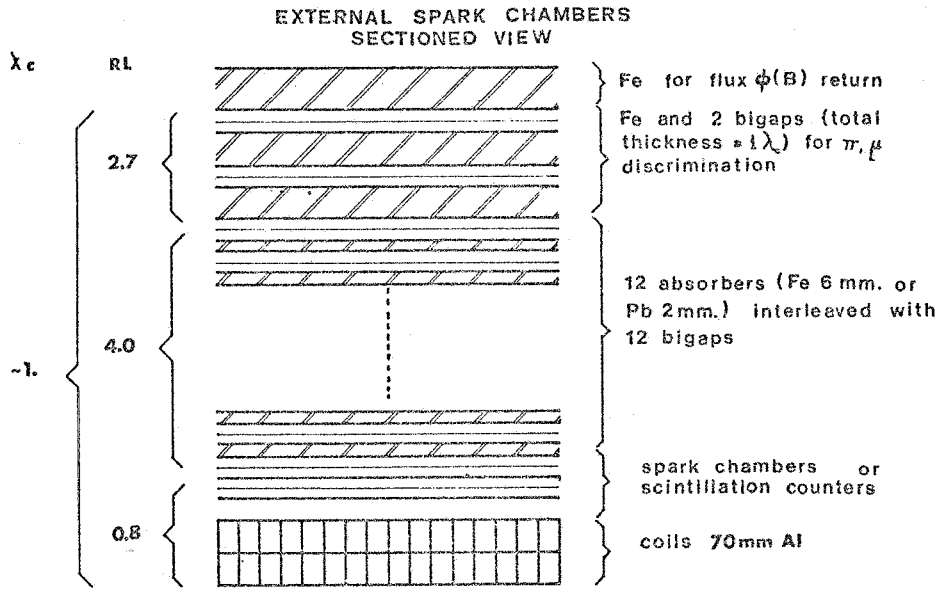

FIG. 6 - Sectioned view of the external spark chambers (λ_c = collision length, RL = radiation length).

c) - Internal Spark Chambers (ISC). -

As distinct from the other parts of the apparatus, which were conceived and designed as fixed or non easily modified components, the internal spark chamber system is flexible and one may choose from many alternatives, the most interesting of which are: a) streamer chambers; b) digital spark chambers; c) conventional cylindrical optical spark chambers with narrow gaps (5-8 mm) or wide gaps (5-10 cm). We have rejected the possibility of using plane-electrode conventional spark chambers, because they do not permit a sufficiently high accuracy in momentum measurement[4].

The alternatives a) and b) are very interesting, nevertheless we thought it advisable to consider in the first phase of the magnet use, only conventional spark chambers, the operation of which is as simple as possible. In this direction we are currently studying two possible solutions.

The first solution (see Fig. 7, Table 4) includes cylindrical wide gap wire spark chambers C2 with large radius of curvature for the observation of trajectories with angles $\delta > 45^\circ$, and plane wire spark chambers C_3 with the electrodes perpendicular to the magnet axis for trajectories with $\delta < 45^\circ$. To choose the spacing between wires some prototypes are under evaluation. Preliminary test results indicate that it is possible to choose a combination of wire diameter (100-150 μ) and spacing (1 ÷ 2 mm) which gives both a good performance of the chambers from the standpoint of distortion and efficiency and a reasonably high optical transparency for viewing through several wire planes[25]. Two small cylindrical spark chambers C_1 with thin gaps (with total plates thickness less than 250 μ), are placed above and below the vacuum pipe and will detect the initial part of the trajectories[5].

The thickness of the material interposed on the entire particle curved path is such as not to introduce a substantial error from multiple coulomb scattering in the momentum measurement[6]. Moreover there is a rather large (1 mm) coherent track displacement in wide gap chambers[14] which, although not interfering with the accuracy of measuring track angles (and hence momentum), decreases their precision in measuring position. For this reason the system also contains 4 narrow gap wire chambers placed at the ends and center of the wide gap chambers arrangement (see Fig. 7c).

The second solution consists of a unique cylindrical spark chamber with many thin gaps able to detect particles to $\delta = 30^\circ$. Light, homogeneous plates can be obtained by glueing aluminium foils ($\sim 10\,\mu$) on expanded polyurethane plates[7]. Since the plates of these chambers are not transparent, one must photograph the direct view of the chambers from a distant point

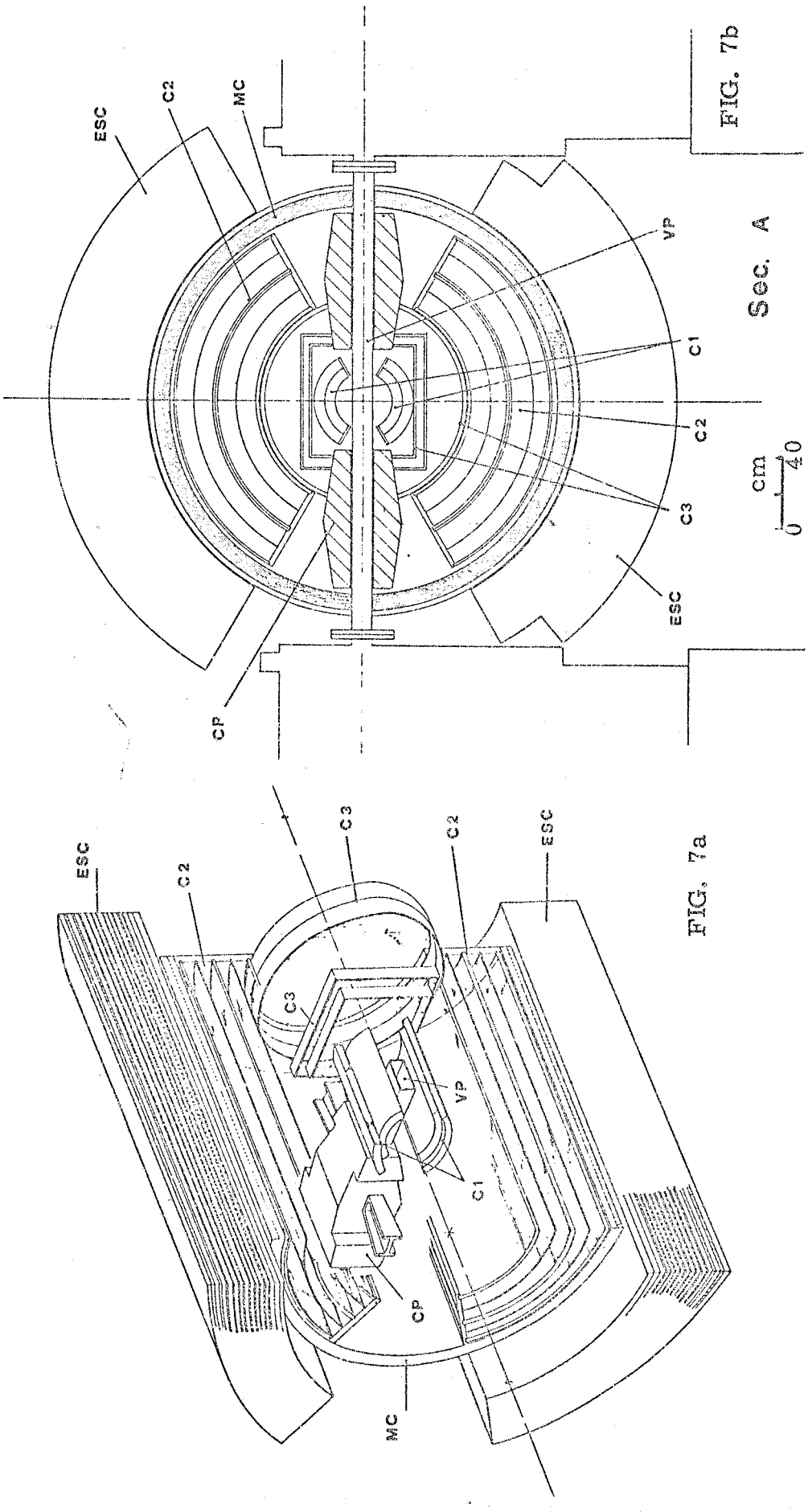

FIG. 7 - External and internal spark chamber arrangement : C1 = internal cylindrical narrow gap spark chamber with thin aluminium plate electrodes; C2 = internal cylindrical wide gap spark chamber with wire electrodes; C3 = internal plane wide gap spark chambers with wire electrodes.

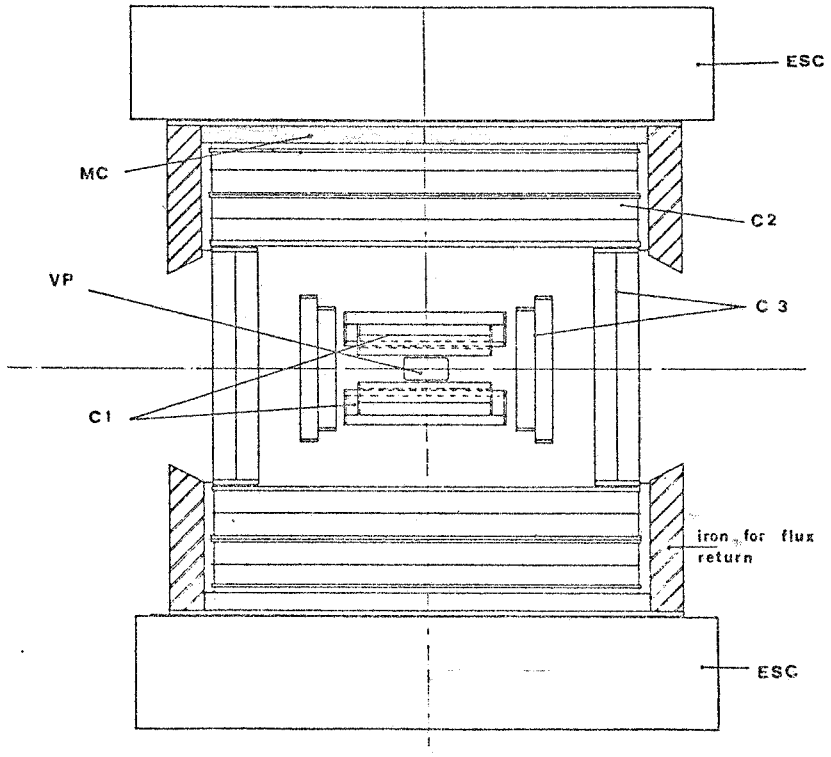

Sec. C

cm
0 40

FIG. 7c

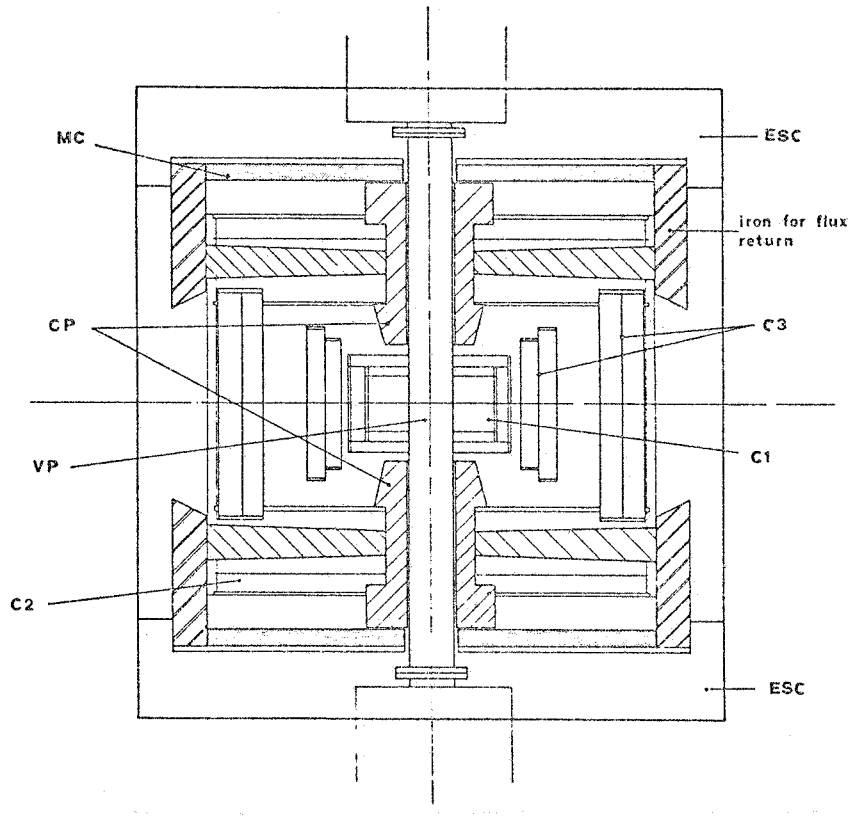

Sec. D

cm
0 40

FIG. 7d

TABLE 4 - Spark Chamber System

a) Internal Spark Chambers (ISC)

Name	C_1	C_2	C_3
Description	Cylindrical, narrow gap and homogeneous plates electrodes placed near the beam	Cylindrical with wire electrodes wide gaps and with narrow gaps placed at the end and center of the wide gaps	Plane, wide gaps with wire electrodes
Angular acceptances	$\psi = 30^\circ - 150^\circ$ $\delta = 30^\circ - 150^\circ$	$\psi = 30^\circ - 150^\circ$ $\delta = 45^\circ - 135^\circ$	$\delta \leq 40^\circ$ $\psi = 0^\circ - 180^\circ$
Dimensions	R_{min} = 150 mm R_{max} = 250 mm Axial length = 700 mm	= 600 mm = 980 mm = 2000 mm	C_3 (first) circular, R = 600 mm C_3 (second) rectangular, 600x700 mm
Gap width	8 mm	100 mm (wide gaps) 8 mm (narrow gaps)	100 mm
N of gaps	8	4 (wide gaps) + 4 (narrow gap)	4
Electrode thickness	250 μ (Al)	wire diameter 100-200 μ wire spacing 1.5-3. mm	as C_2
Total gas volume in the ISC	2000 liters		

b) External Spark Chambers (ESC)

Description: cylindrical bigap spark chambers(with reflecting aluminium plates)interleaved with iron or lead

Angular acceptance: $\psi = 30^\circ - 150^\circ$
$\delta = 45^\circ - 135^\circ$

Dimensions: R_{min} = 1100 mm
R_{max} = 1650 mm
Axial length = 2600 mm

Gap width: 8 mm

N. of bigaps: 10 - 15

Electrodes thickness: see sectioned view of the external chamber system Fig. 6

Total gas volume: 3500 liters

requiring that the iron flux-return plates either be removed or cut in many places to allow visibility (see Fig. 10a). This modification implies a 20% decrease in the mean magnetic field and the introduction of field inhomogeneities.

As mentioned above both these solutions seem a priori possible and will be studied when the necessary prototypes are ready. In the assembly drawings of the apparatus and in the following discussion we have considered only the first solution which, if feasible, is more accurate.

d) - Trigger Counter System. -

The trigger counter system consists of three layers of scintillators: the first two (S_1, S_2) are placed between the vacuum pipe and the first spark chamber C_1, and the third (S_3) can be placed internally just under the main coil (between it and the internal C_3 spark chamber) or above it, before the external spark chamber. The best solution will depend essentially on machine background.

The number of counters S_{3j} in the third layer was selected such that two particles with an opening angle greater than $\sim 15^\circ$ will always produce signals in two distinct scintillators of this layer, i.e. a net four-fold coincidence (see Fig. 8). The general data on the system are collected in Table 5 and in Fig. 8 and 9.

TABLE 5 - Counter System

Trigger counters internal to the magnet: 2 layers for a total of 8 scintillation counters, placed around the vacuum chamber (see Fig. 10); scintillator dimensions are 200x300x10 mm^3 and 100x300x10 mm^3; number of photomultipliers (placed externally to the flux return plates) is 8.
Trigger counters external to the magnet main coil: 1 layer of 14 scintillation counters placed around the main coil (see Fig. 10) with dimensions 300x2600x25 mm^3 each; the total number of photomultipliers is 28.

The trigger logic will depend on the kind of events to be detected: the most unfavorable case from the point of view of background is the reaction

$$e^+ e^- \rightarrow X^+ X^- Y^o$$

with the two charged trajectories both above (below) the plane of the storage ring. For this kind of events the trigger logic will be (see Fig. 8c)

$$(S_1 S_2 S_{3j} S_{3k}) + (S'_1 S'_2 S'_{3j} S'_{3k}) \qquad j \neq k$$

For two charged collinear tracks the following conditions have to be imposed (see Fig. 8a)

$$S_1 S'_1 S_2 S'_2 S_{3k} S'_{3k}$$

Obviously other kinds of logic can be found for more complex events.

It is possible that the system will not be sufficiently selective at least for the most unfavorable logic configurations if Adone gives a high background level.

The choice of the improvements to make in the trigger system will clearly depend on the nature of backgrounds. In particular the rejection of showers generated from beam interactions with the residual gas and with the walls of the vacuum chamber can be improved by increasing the angular subdivision of the first and second counter layer.

Moreover we retain the possibility of inserting counters in place of some external bigaps to include in the logic the requirement of coincidences with γ conversion products

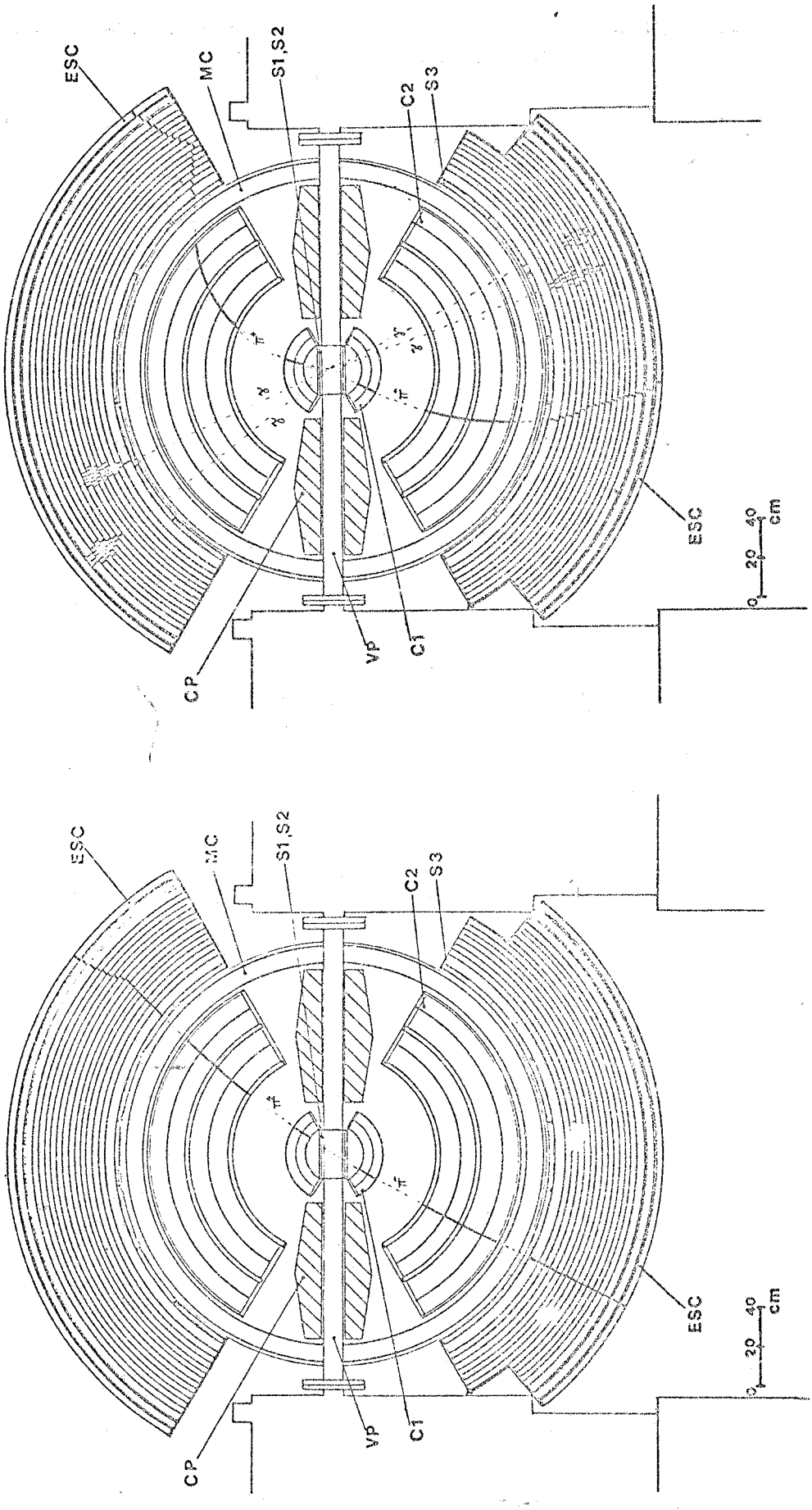

FIG. 8 - Examples of some typical e^+e^- reaction as seen in the front view of the apparatus.

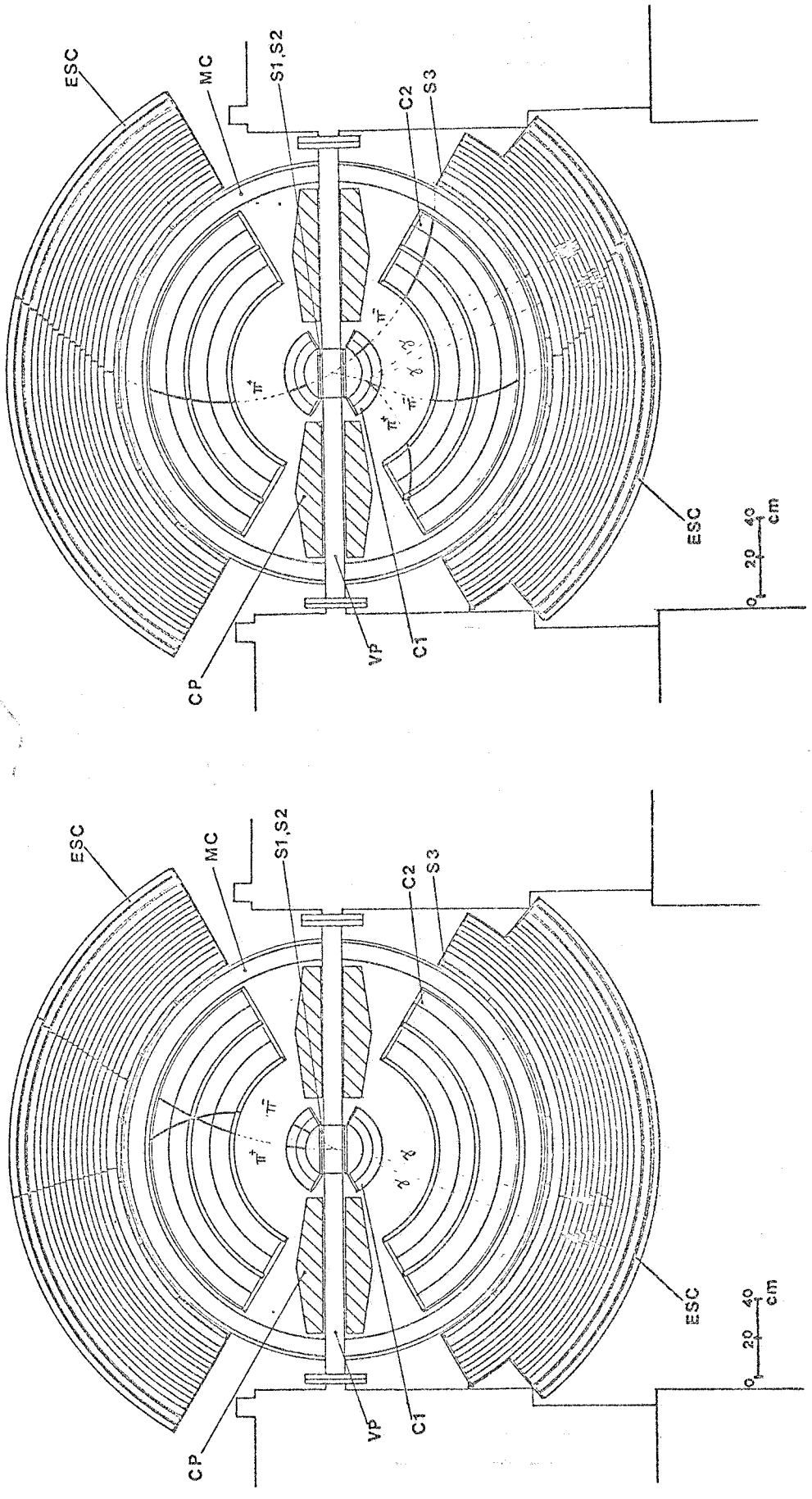

FIG. 8 - Examples of some typical e^+e^- reaction as seen in the front view of the apparatus.

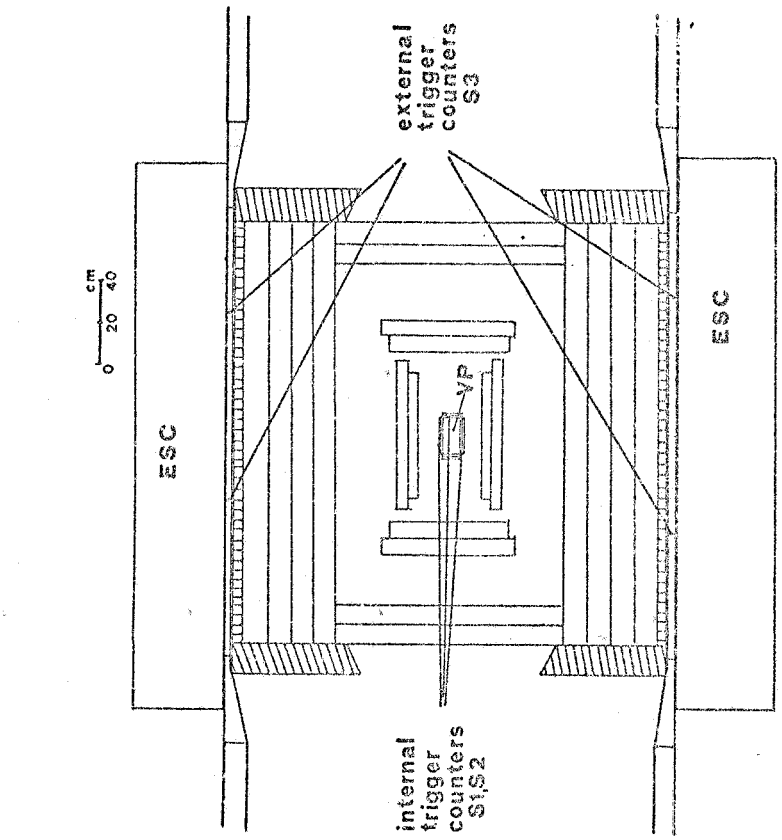

FIG. 9b

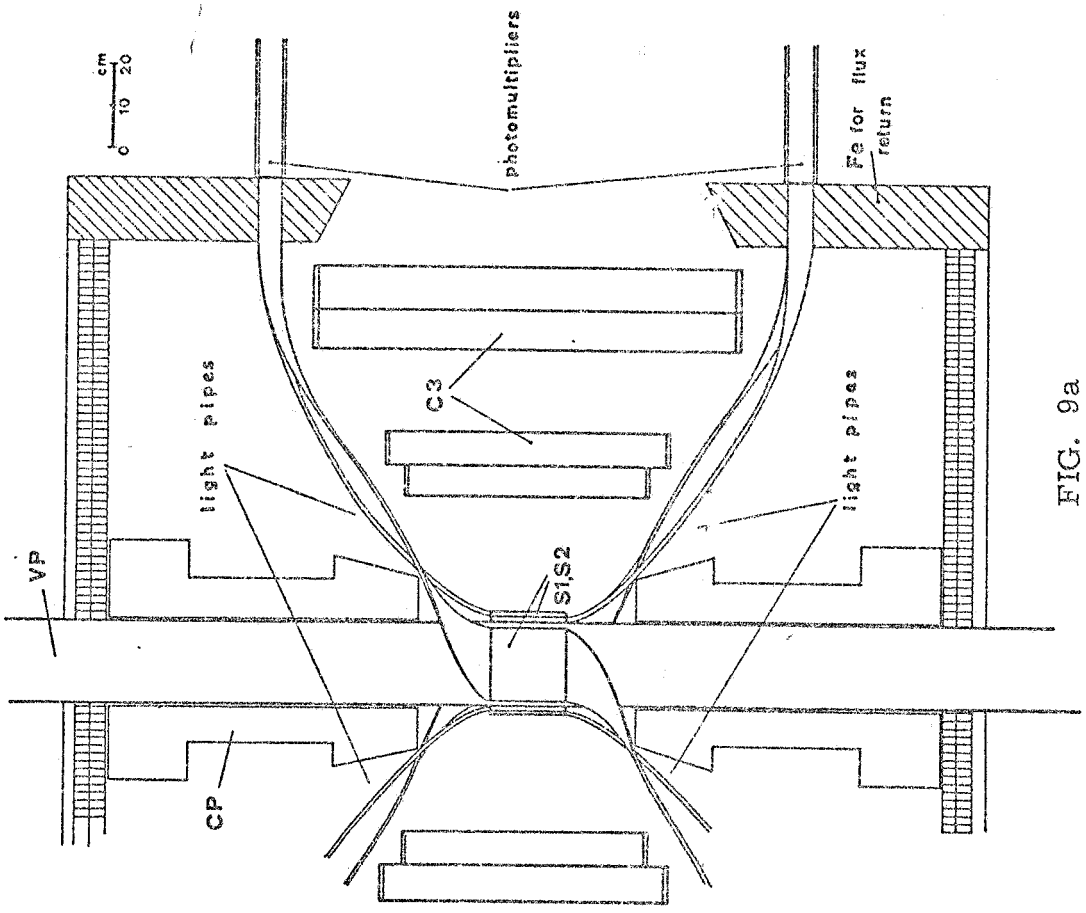

FIG. 9a

FIG. 9 - Trigger counter system.

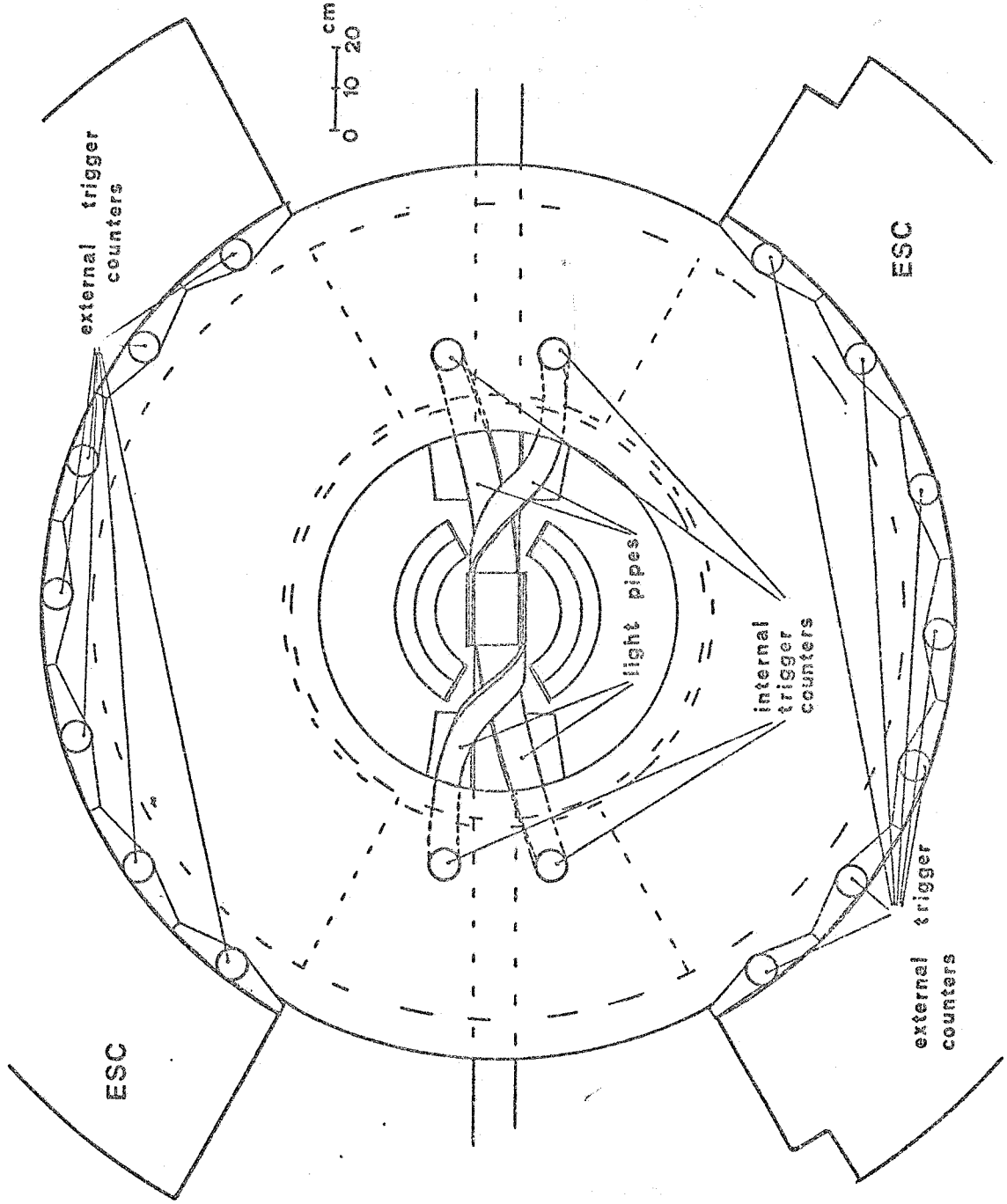

FIG. 9 - Trigger counter system.

for events as

$e^+ e^- \rightarrow$ charged + (γ) ; $e^+ e^- \rightarrow$ charged + (π^0).

e) - Optics. -

The internal spark chambers are seen from two cameras placed on the magnet axis (see Fig. 10a, b). In this way all the internal space is visible on at least one picture (70 mm film). The sparks in the internal spark chambers are observable through their transparent plates. In Fig. 11 is shown the appearance of the trajectories on the film, from which can be seen the dependence of the image on the emission angle, δ. This dependence allows the complete stereoscopic reconstruction of the events with only one camera (two cameras are necessary only for the field view limitation due to the iron plates at the ends of the main coil and to the walls of the spark chambers[8]).

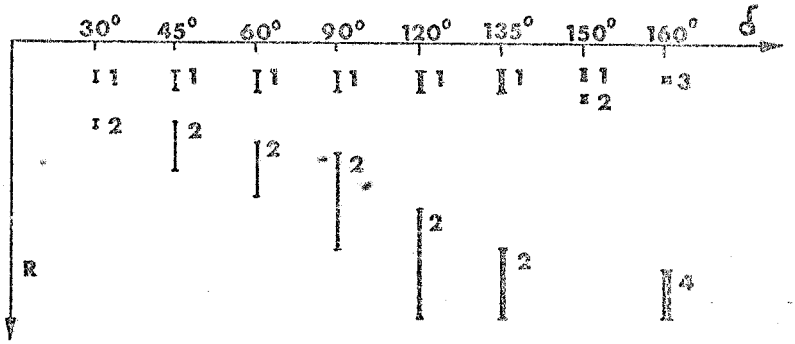

FIG. 11 - Relationship between the δ angle of a track and the spark length on the picture and the distance R of the sparks from the center of the picture.

The optical path distance was chosen to allow the reconstruction of the spark space position with maximum accuracy in both coordinates.

An optical system for the external spark chambers is shown in Fig. 10; the mirror system was arranged to allow photographing of the external and internal chambers by a single 3 lens camera (see Fig. 10). A more straightforward optical system in which two direct views of the external chambers are used to give stereoscopic spark information is under study. This method also would result in two cameras viewing all chambers.

The most important parameters of the optics are collected in Table 6.

TABLE 6 - Optics

Number of cameras:	2	
Number of lenses:	2 x 3 = 6	
Lens characteristics:	for ISC	for ESC
Focal length	~ 40 mm	~ 340 mm
Optical path length	m	20 m
Angular aperture	60°	17°
Lens aperture	f/11	f/11
Demagnification	50	60
Field depth	2 m	2.6 m
Image characteristics:		
Horizontal dimension	40 mm	50 mm
Vertical dimension	40 mm	35 mm
Circle of confusion diameter	40 μ	40 μ

The image format is compatible with the automatic scanning machines of CNAF (the Italian national scanning facility). See Fig. 11 for more details.

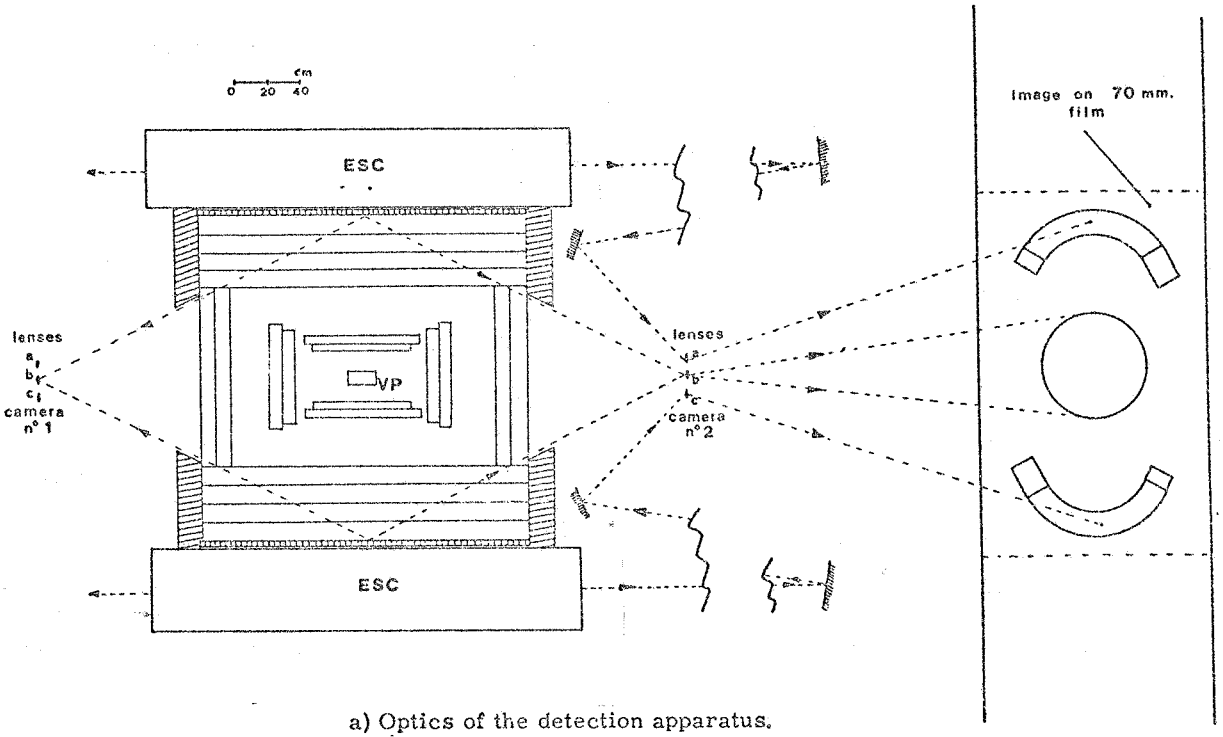

a) Optics of the detection apparatus.

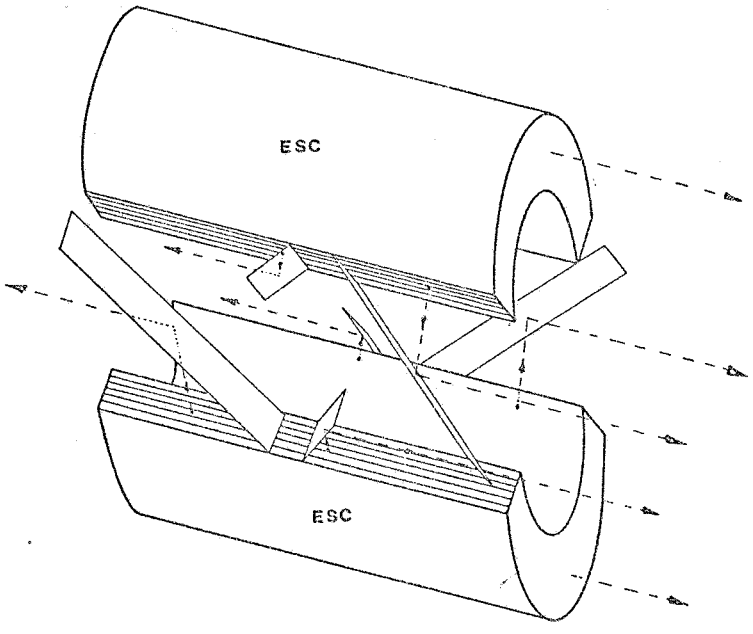

b) Mirror system for the side view of the external spark chambers.

FIG 10

f) - Monitor. -

The actual apparatus allows the simultaneous use of the three kinds of luminosity monitors proposed up to now in first generation Adone experiments:

1) γ detection at 0° and 180°;
2) elastic e^+e^- scattering at small angles ($\theta \sim 4^\circ \cdot 5^\circ$);
3) elastic e^+e^- scattering in the angular interval of the apparatus ($\theta \gtrsim 30^\circ$).

The use of these monitors should be considered separately for each reaction or group of reactions studied, in connection with the beams, the accuracy requirement and the stability of the interaction region.

The experience obtained in the first generation experiments in Adone will be very useful for a final choice.

g) - Electronics. -

We consider as an integral part of the magnetic system that part of the electronic equipment which will be common to all experiments. In particular:

a) power supply for counters and spark chambers (see Table 7);
b) fast logic for spark chamber triggers. This consists of a rejection system for cosmic rays based on time of flight measurements[9], the coincidence with the master impulse of the machine and logic to obtain coincidences of two or more charged tracks (see Fig. 12). The list of components is given in Table 8;
c) monitor logic.

The data recording and reduction systems will be defined by the particular experiments.

TABLE 7 - Power supply

a) Spark chambers power supply	
External spark chamber capacity	30×13000 pF $\simeq .4$ μF
Marx generator capacity for wide gaps	.1 μF
Recover time of the spark chambers	$\gtrsim$ 1 sec
Charge current	$\simeq$ 5. mA
b) Photomultiplier power supply	
36 photomultipliers (see Table 5):	I_{tot} = 36 mA at a voltage $\sim$2500 V

TABLE 8 - Electronics

1	GTM	Dead time generator
4	FIL	Linear fan-in
4	FO	Fan-out
6	GNLR	Logic gate
4	CRR	Fast coincidence
1	TRR	Fast trigger
3	TRL	Slow trigger
18	DR-SF	Fast discriminator with fixed threshold
3	DR-SV	Fast discriminator with variable threshold
19	RV	Variable delay
1	AR	Resistive attenuator
1		Binary scaler
24		Flip-flops
2		Decimal scalers

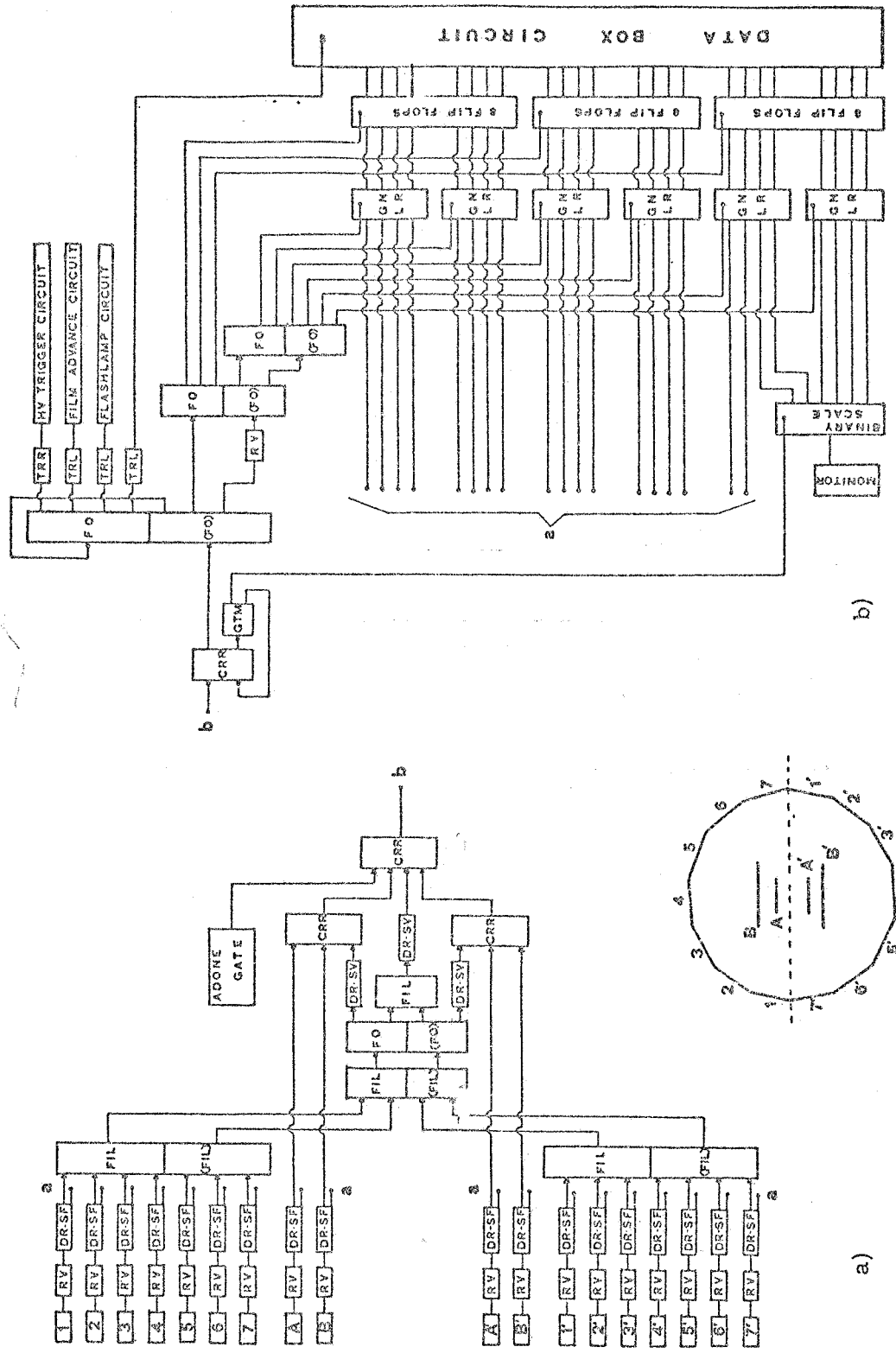

FIG. 12 - Block diagram of the electronics for a 2 or more charged particle coincidence.

h) - Gas Control System. -

The large volume and high purity of neon gas necessary for proper spark chamber operation have dictated the design of a fail safe gas purification equipment with high flushing velocity and versatility. The main features of this system are described in § X.

i) - Straight Section. -

To minimize the compensator gap height and to eliminate obstacles from the largest possible area around the interaction region, a straight section with a peculiar shape was designed. The vertical dimension is determined by the shift introduced by the magnetic field on the principal orbit of Adone (see Fig. 13).

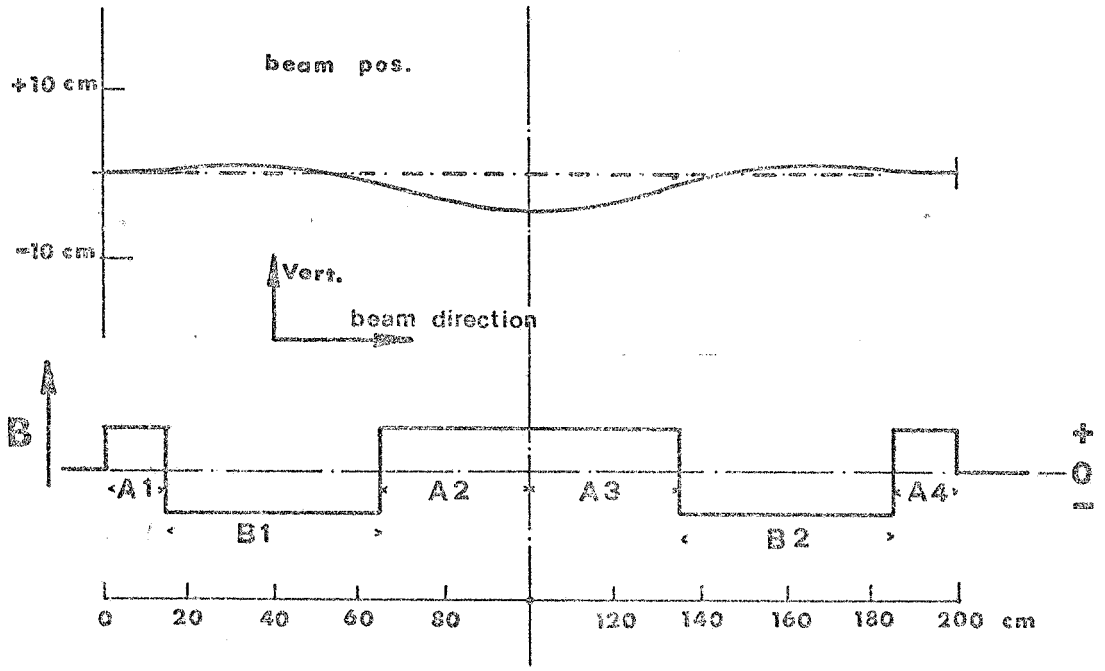

FIG. 13 - Qualitative behaviour of B as a function of z and the electron orbit in the vertical plane (the vertical scale is magnified by a factor 2).

l) - Support Frame for the Magnet. -

In order to allow easy access to the Adone vacuum chamber and to the internal detection apparatus, the solenoid must be separated along a plane perpendicular to the magnet axis at the center, with the two halves then being drawn apart. The magnet, the detection apparatus and the support system must all be consistent with this requirement (see Fig. 5).

III. - MAGNETIC INTERFERENCES WITH ADONE. -

The magnetic system described in the previous chapter satisfies the conditions

(6) $$\int B\, ds = 0 \qquad\qquad B(-s) = B(+s)$$

The variation of B along z is qualitatively shown in Fig. 13; in the segments A_1, A_2, A_3, A_4 the field B is that of the main coil, whereas B_1, B_2 correspond to the compensators. Each compensator consists of two coaxial coils N_1, N_2 (see Fig. 4e) generating, in absence of edge effects, an opposite magnetic field on 50% of the beams path, keeping uniform the external field. The field uniformity inside and outside the compensators is obtained interposing some iron between N_1 and N_2 which acts as a shield preventing the flux generated

by the main coil from linking itself with the beam. Hence the coil N_2 is placed in a zero field cavity and its field is perfectly uniform. As the lateral flux (see Fig. 4a) generated by N_1 is nearly zero, also the field outside N_1 and N_2 will be uniform.

The position of the compensators, chosen to minimize their angular dimensions and the perturbation on the orbit in the segments B_1 and B_2(6), is such that:

$$l(A_1) = l(A_4) = 15 \text{ cm} ; \quad l(A_2+A_3) = 70 \text{ cm} ; \quad l(B_1) = (B_2) = 50 \text{ cm}.$$

The orbit in the vertical plane is shown in Fig. 13 (the vertical scale is magnified by a factor two) for $E_{beam} = 300$ MeV in the extreme case that at this energy the field B can be set at the maximum value of 4.5 kG. In these conditions the vertical perturbation of the orbit at the exit of the compensators has a maximum displacement of 1.75 cm. The perturbation has a maximum at the center of the straight section: the displacement of the interaction point is about 1 cm at 1.5 GeV and 5 cm at the injection energy (375 MeV), where it is not necessary to work with maximum intensity of the magnetic field anyway.

The size at the compensator yoke depends on the saturation value of the iron employed (13-18 kG); hence the value for α below which the compensator is an obstruction could vary from 38° to 34° in the final design. The gap of the compensator coils is wider in the region of maximum beam displacement. The total power absorbed by the compensator coils is 300 kW.

We provide a variable shunt for fine current adjustment to accurately satisfy the condition of zero field integral.

Many perturbation effects have been calculated; we report here the main results. The details can be found in the Internal Memoranda.

Closed Orbit Displacements. -

It can be easily shown that the closed orbit displacements outside the straight section, is zero everywhere if the conditions (6) are satisfied(10).

Radial-Vertical Coupling. -

As the magnetic field is transverse, a coupling of vertical and radial betatron oscillations is introduced only through the field non uniformities which generate longitudinal components. Coupling effect were calculated with the conclusion that rather strong longitudinal fields ($\sim$ 1 kG) can be accepted without danger over the whole straight section; we can assume then that in our case they are completely negligible.

Non Linear Effects. -

A dependence of the betatron oscillation frequencies on the amplitude would be introduced if the magnetic field had an important octupole component. Such field components would be present in the fringing fields of the compensators and of the solenoid itself. Since the aspect, dimensions and field strengths at these points are quite similar to that of an Adone bending magnet, we expect the octupole components presented by the solenoid and the compensators to be comparable to those given by the Adone structure. A Adone is not severely affected by the presence of 24 fringing fields of the latter type, we expect no problem from those of our magnetic system. Moreover the pole shapes of the compensators can be machined during the assembly (as for the Princeton-Stanford ring) to eliminate the octupole components if necessary.

Effects on the Vertical Plane. -

The effects of the field in the vertical plane, in a linear approximation, are reduced to an increase of the effective length of the straight section. This effect for B = 4.5 kG is small at all energies (at most $\Delta l = 2$ cm) and within the machine tolerances.

Field Integral Compensation. -

The field integral compensation will ultimately be made to some non zero value. We consider here what that precision must be if the Adone beam is not to be destroyed by the net impulse received from the magnet on each turn. Choosing a .1% deviation in the correct field value in one of the compensators, we have calculated the displacement in equilibrium orbit around the machine.

We obtain, for a maximum vertical beam displacement, 1.6 mm assuming full field in the solenoid and injection energy. At peak energy, this drops to .3 mm. In view of the 5 cm vertical half aperture of Adone and realistic experimental requirements on the accuracy in the position of the interaction point, this result is quite satisfactory. The required compensation accuracy than is $\sim$ .1%, or $\sim$2 gauss-meter, the figure assumed in the design.

Radial Lens Effect. -

The shape of the equilibrium orbit in the magnet (see Fig. 13) results in a non normal entry of the particles into the fringe fields of the compensators. This in turn causes a focussing action in the radial plane, the focal length of which varies as the square of the ratio of beam momentum to magnetic field. With full magnetic field at injection this focal length is about 2.8 meters, to be compared with a focal length of the quadrupole pairs of 6.4 meters; hence the extra focussing is very strong compared to the focussing of the machine itself and is a serious perturbation.

The effect of such an insertion is threefold: an increase in the number of radial betatron oscillations, an equal broadening of the stop band width, and an increase in the radial betatron amplitude function β_R. The first two effects, essentially, result in an unstable machine below 400 MeV/beam, but well before this point, at 1000 MeV/beam, the amplitude function has increased by 15%, implying a decrease in luminosity of this order. Taking this as a maximum tolerable effect, we have the result that the field of the experimental magnet must be reduced in proportion to the beam momentum below 1000 MeV/beam. By reducing the current in the focussing and defocussing machine quadrupoles immediately adjacent to the straight section, these radial effects can be completely eliminated. In doing so however, one introduces similar changes in the vertical plane but at least a factor of four smaller (see Fig. 14). This implies that the limiting energy for operation at full field is now at 600 MeV/beam. Furthermore, the additional corrections necessary to compensate for the vertical disturbances left at this point are of the order of those expected in normal machine tuning; hence, we may confidently expect that there will be no non-easily correctable interference with the machine by the experimental magnet. Details on the radial lens effect and field integral compensation may be found in an internal memorandum[24].

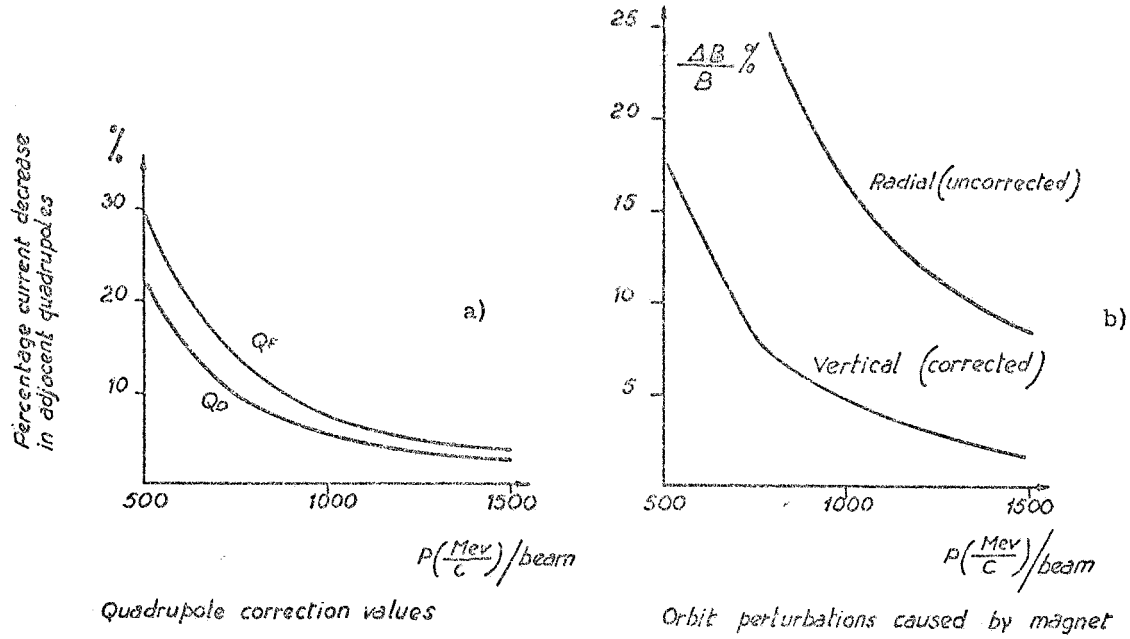

FIG. 14 - The magnetic structure of Adone consists of $(B/2)Q_D Q_F S Q_F Q_D (B/2)$ where B/2 is one half of a bending magnet, S the straight section and Q_F and Q_D are the radial focussing and defocussing quadrupoles.

IV. - ACCEPTANCE OF THE SPARK CHAMBER SYSTEM. -

a) - Connection between geometrical acceptances and detection efficiencies for multibody reactions. -

In a reaction with N bodies the directions of the emitted particles are in general correlated because of the spin dependence of the reaction matrix elements, the final state interactions and the conservation of energy-momentum. In order to optimize the detection apparatus it is useful to calculate the detection efficiency of some ideal reactions for which all of the following statements are true.

1) The e^+e^- polarization effects are negligible.

2) The kinematical correlations due to energy-momentum conservation among the N-1 detected particles of N product particles are negligible. This condition is practically satisfied by many real e^+e^- processes.

3) There are final state interactions. Possible interactions are considered either so weak as to produce no correlation at all, or so strong that M of the N final state products are emitted collinearly and can be regarded as a single particle in the efficiency calculations. Examples of this latter type are the γ's of decaying π^0 with $E_{\pi^0} \gg m_{\pi^0}$ and the decay products of a narrow resonance in which the ratio between the kinetic energy of the resonance and the Q value of its decay is very high.

Naturally among real processes some will be very similar to the corresponding ideal processes and others can be very different: their detailed analysis will be the object of particular research programs. Nevertheless we think that from the standpoint of optimizing the experimental apparatus for a large class of experiments it will be sufficient to take into account the geometrical efficiencies calculated only for the ideal processes mentioned above.

If C neutral and K charged particles are produced in a reaction we distinguish two cases:

a) $K \neq 0$, $C = 0$. In this case we require the detection of K-1 of the K charged products. Then the efficiency is:

$$\eta(\varepsilon_K) = \binom{K}{K-1} \varepsilon_K^{K-1}(1-\varepsilon_K) + \varepsilon_K^K = K\,\varepsilon_K^{K-1} - (K-1)\,\varepsilon_K^K \tag{7}$$

where ε_K is the acceptance of the system for the detection and the momentum analysis for charged particles.

b) $K \neq 0$, $C \neq 0$. We require the detection of all charged and of C-1 neutral products. Then:

$$\eta(\varepsilon_K, \varepsilon_C) = \varepsilon_K^K \left\{ \binom{C}{C-1} \varepsilon_C^{C-1}(1-\varepsilon_C) + \varepsilon_C^C \right\} \tag{8}$$

where ε_C is the acceptance of the system for neutral particle detection. Fig. 15 shows the dependence of $\eta(\varepsilon_K, \varepsilon_C)$ with ε_K and ε_C for some typical values of C and K, in the two cases given by (7) and (8). From the curves shown in Fig. 15 we have obtained the minimum acceptable value of the parameters ε_K and ε_C for the apparatus. In particular requiring $\eta \geq .25$ for 3 and 4 body reactions we have obtained $\varepsilon_K \geq .50$ and $\varepsilon_C \geq .45$.

b) - Acceptance of the System: Internal Spark Chambers. -

In Fig. 16 we have represented the areas of solid angles covered by the different parts of the apparatus on a cylindrical surface S, geometrically similar to the actual solenoid: the areas E and F are covered respectively by the cylindrical and plane spark chambers. The area C represents the obstacle of the compensator projected on S from the origin. The areas A and B are covered by mechanical supports, cooling pipes and electrical connections. Finally D is a free area, but very difficult to cover with a simply shaped spark chamber.

A conformal representation of these parts of S in the cartesian plane (θ, φ) is shown in figure 17a. As in this figure, the areas are proportional to the solid angles covered, the dependence of the acceptance of the different parts of the system on the θ and φ angles can be easily deduced. The acceptance of the internal chambers (regions E and F) integrated over φ as a function of the θ angle is shown in Fig. 18.

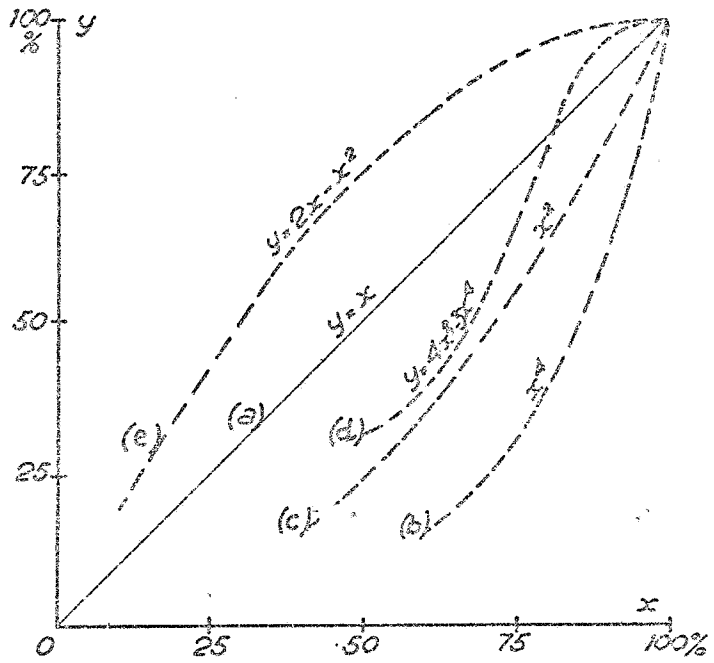

FIG. 15 - Dependence of the detection efficiencies on the solid angle for various reactions (see formulas (7, 8), § IV): a) with 2 charged tracks; b) with 4 charged + 1 neutral track; c) with 2 charged + 1 neutral track; d) 4 charged tracks; for these curves $x = \varepsilon_K$; e) reactions with K charged and 2 neutral particles: probability of detecting one of the two neutrals. In this curve $x = \varepsilon_C$. For reactions, 2 charged + 2 neutral, the efficiency is $\eta = y(c) \cdot y(e)$, and for reactions 4 charged + 2 neutral is $\eta = y(b) \cdot y(e)$.

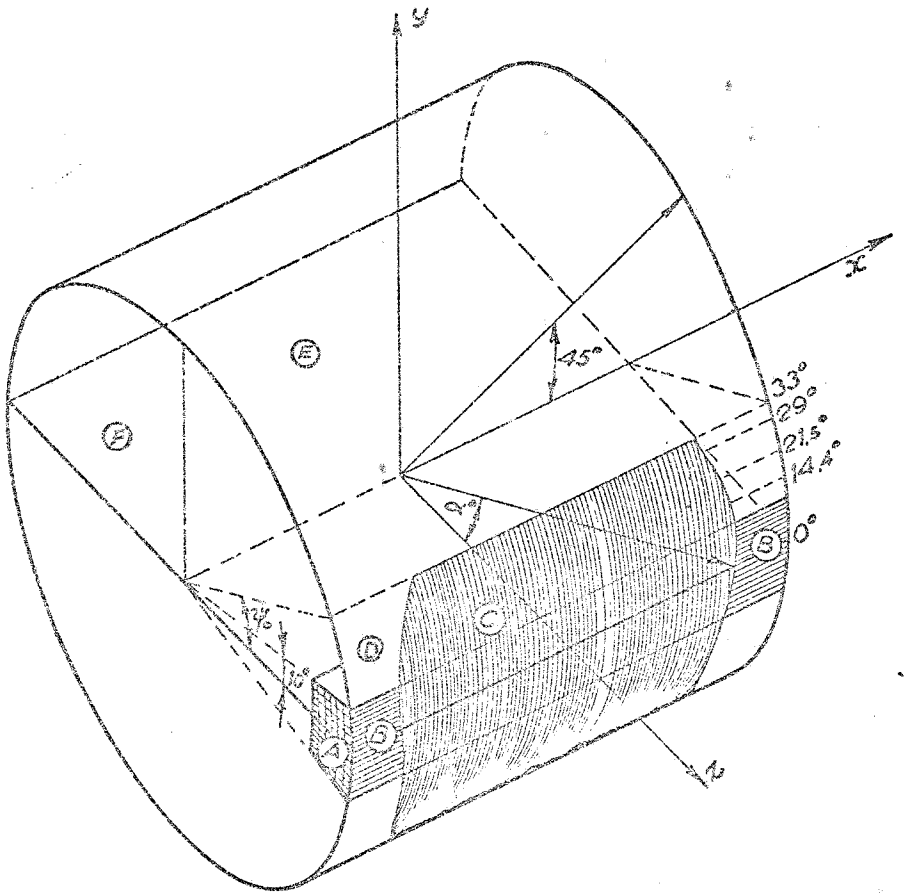

FIG. 16 - Subdivision of the cylindrical surface S (§ IV). The area C is the shadow of of one compensator, A and B are shadows due to the water cooling pipes and electrical connections. The areas D, E and F are free for particle detection.

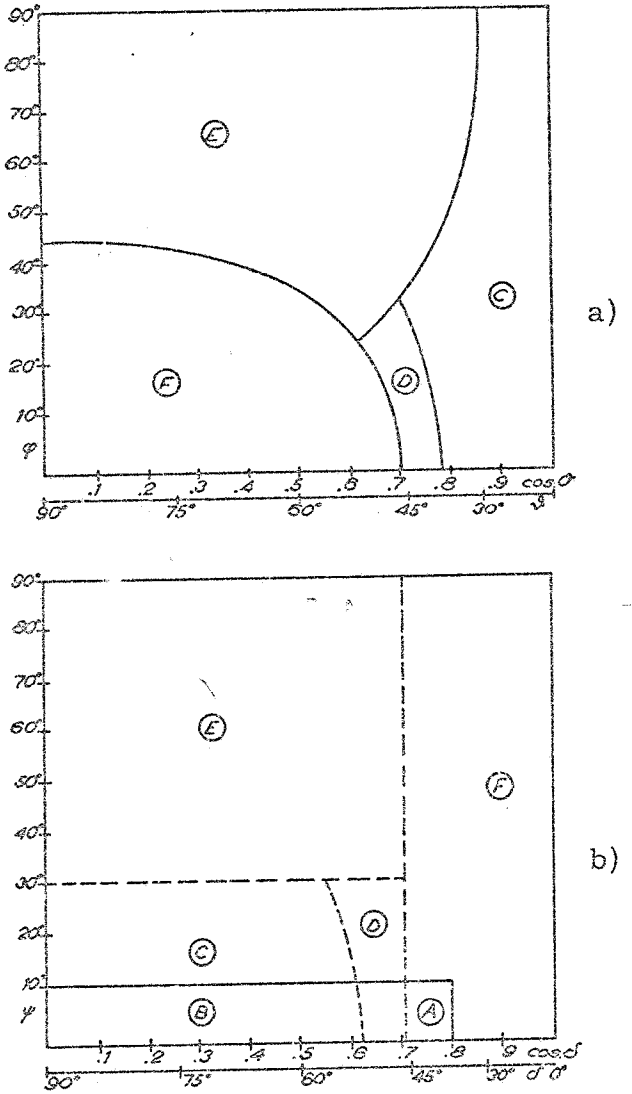

FIG. 17 - a) conformal representation in the (θ, φ) plane of the areas shown in Fig. 16; b) conformal representation in the (δ, ψ) plane for the areas shown in Fig. 16.

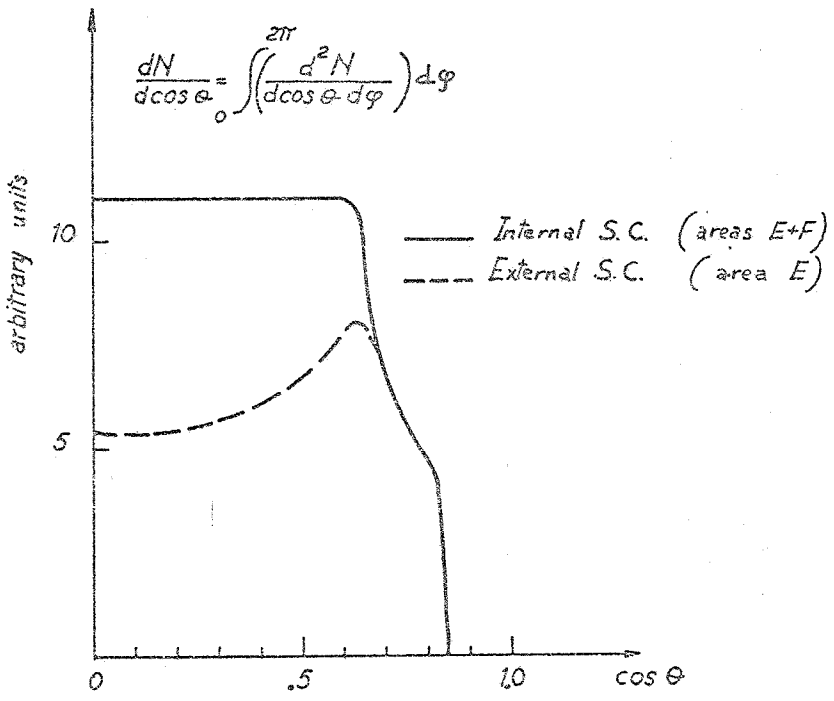

FIG. 18 - Acceptances of the internal and external spark chambers integrated over φ as a function of θ.

The integrated acceptances are:

$$\varepsilon_E = .47 \; ; \qquad \varepsilon_F = .13 \; ; \qquad \varepsilon_K = \varepsilon_E + \varepsilon_F = .60$$

We point out that the momentum analysis will be possible in a solid angle slightly smaller than the one covered by the chambers. In fact for small δ angles the error on the momentum increases rapidly going to infinity for $\delta \to 0^o$. If we exclude the momentum measurement for $\delta < 10^o$ (see the following paragraph on the discussion of this value) we find: $\varepsilon_K = .59$.

c) - Acceptances of the System: External Spark Chambers. -

The external spark chambers cover the part E of the surface S: the integrated acceptance is

$$\varepsilon_C = \varepsilon_E = .47$$

The dependence of the φ integrated acceptance on θ angle is shown in Fig. 18.

d) - Detection Efficiency. -

With the values ε_K and ε_C for our apparatus[11] and with the suitable formula (7) or (8) we calculated the detection efficiencies for some typical reaction, idealized as mentioned above; the results are shown in Table 9.

TABLE 9 - Acceptances of the Transverse Arrangement

Reaction Multiplicity	Example	$\eta(\varepsilon_K, \varepsilon_C)$	Notes
K = 2, C = 0	$\pi^+\pi^-$	0.70	Taking account of $\sin^2\theta$ dependence
K = 2, C = 1	$\pi^+\pi^-\pi^o$ ($E_{\pi^o} \gg M$)	0.36	Observing $\pi^+\pi^-$ with $\delta \geq 45^o$
K = 4, C = 0	$2\pi^+ 2\pi^-$	0.45	Observing 3 charged particles
K = 4, C = 1	$2\pi^+ 2\pi^- 2\pi^o$ ($E_{\pi^o} \gg M$)	0.13	Observing $2\pi^+ 2\pi^-$
K = 2, C = 2	$\pi^+\pi^- 2\pi^o$ ($E_{\pi^o} \gg M$)	0.23	Observing $\pi^+\pi^-\pi^o$

In some cases (reactions $\pi^+\pi^-\pi^o$ and $\pi^+\pi^+\pi^-\pi^-$) the efficiencies were calculated using Montecarlo techniques and properly taking into account the kinematical and the initial state effects; very little difference was found from the tabulated values.

V. - SPATIAL RESOLUTION. -

In this and in the next paragraphs we will examine the accuracy of the apparatus for charged particle detection. We will discuss here the limits on the spatial resolution of a single spark. In the following the errors on the parameters defining a trajectory (p, δ, φ) and the resolution obtained in two typical multibody reactions $e^+e^- \to \pi^+\pi^-\pi^o$ and $e^+e^- \to \pi^+\pi^+\pi^-\pi^-$ will be discussed. In the first reaction a final particle is not detected (π^o), in the second all the final products are detected[12].

In all of these considerations we have assumed those dimensions of the interaction region which are predicted for Adone under normal operating conditions, i.e. with beams crossing at an angle in the interaction region.

a) - Spark Jitter. -

It is possible to correct for the lateral displacement of each spark in the direction $\vec{E} \times \vec{B}$, which is of the order of $1 \div 1.5$ mm both for narrow and wide gap spark chamber[13,14]. We have only to discuss the inaccuracy introduced by the spark development mechanism which produces incoherent fluctuations in the spark position (jitter).

For narrow gap spark chambers ($\sim$7 mm) the importance of this effect has been studied and has been found to depend on the angle of the track to the electric field. This dependence is expressed by the following empirical formula:

$$\sigma_y = (0.30 + 0.44\,\psi)\ \text{mm} \qquad \psi \text{ in rad} \qquad 0 \leq \psi \leq 1$$

where σ_y is the fluctuation perpendicular to the electric field and to the optical axis and ψ is the azimuthal angle of the trajectory with respect to the optical axis, with the condition that the normal to the plates has $\psi = 0$[13], i. e. the electric field is parallel to the z-axis of Fig. 1.

For wide gap spark chambers with plane electrodes these fluctuations seem to be much lower. For tracks parallel to the electric field, that is with ψ angle less than 10°, the fluctuation σ_y, on a mean track segment of 2.5 cm, is 0.06 mm[14]. As far as we know there are no convincing data on inclinations greater than 15°, nor data of this kind on spark chambers with wire electrodes (transparent wide gap).

b) - Distortions of the Optical System. -

The optical distortions caused by the lens and the mirrors are, at least in principle, completely correctable. One must only take a picture of a fiducial mark system whose spatial position is accurately know (see the following point c)) and reconstruct it in real space. On the basis of the previous experiments[13] we expect the resulting corrections to be small and with little error.

c) - Position of Fiducial Marks. -

The fiducial mark system is obtained by precisely inscribing lines ($\pm 25\mu$) on transparent plates. The spatial position of the fiducial marks will be known independently from the photographic system, by optical measurements to an accuracy of the order of $100 \div 150\mu$ in space[15].

d) - Errors due to the Photographic and Measuring Systems. -

The spark brightness in a wide or narrow gap spark chamber is sufficient for a diaphragm opening K = 16 (f/number)[13,14]. A bright point produces on the film a circle of confusion due to the diffraction and to the field depth. If we require the two circles of confusion to be equal, a demagnification I = 50 has to be used for a field depth of 2 meter and $\lambda = .6\mu$. For this value the diameter of the two circles of confusion is about 25μ.

Measuring the sparks with an FSS (Flying Spot Scanner) system it should be possible to locate the spark center with an accuracy of 1.6μ on the film. Nevertheless, given the presence of the confusions caused by the diffraction and by the field depth and of the film resolving power, it is likely that the center of a 40μ point on the film will be located with $2 \div 3\mu$ accuracy. So the spark position in a plane perpendicular to the optical axis will be located with an error $\sigma_y = 100 \div 150\mu$ caused by the measuring apparatus. Evidently the depth spark position, which is along the optical axis, will be determined with an error σ_x which will depend on the stereoscopic factor A : $\sigma_x \simeq \sqrt{2}\, A\, \sigma_y$ (in our case $A \simeq 3$).

e) - Conclusions on Single Spark Errors. -

For narrow gap spark chambers the errors caused by spark incoherent fluctuations ($\sim 300\mu$) dominate the errors of the fiducial mark positioning ($\sim 150\mu$) and the measurement errors ($\sim 150\mu$).

While the 300μ jitter for narrow gap spark chamber is well confirmed and easily obtained, the value for wide gap chamber depends appreciably on working conditions (gas purity, high voltage pulse characteristics, clearing field value). To give a total error, with the same degree of reliability as for narrow gap spark chambers, we are studying the behaviour of wide gap prototypes.

As the only difference between a conventional and a wire electrode spark chamber is a non uniformity of the electric field in regions which are a very small percentage of the total track length, we expect a jitter certainly smaller than 300/μ with perhaps a lower limit of 60/μ as measured in other laboratories[14] with homogeneous electrode wide gaps. If this value is confirmed the total error of these chambers will be determined essentially by the optics and by the measuring apparatus.

VI. - MOMENTUM AND ANGULAR RESOLUTION. -

As seen in the previous paragraph, the accuracies for wide gap and narrow gap spark chambers are quite different. The narrow gap spark chambers were extensively used in physically interesting[13] measurements and the calculated resolutions agree with the experimental distributions. In the case of wide gaps the accuracies are still not sufficiently checked, especially in the wire electrode case.

Hence, first we will derive values for the accuracy of momentum and angular measurements using the more reliable, but less favorable, experimental arrangement, i.e. narrow gap chambers. We will discuss later the improvements we think can be achieved using wide gaps instead.

In the calculations we assumed a constant magnetic field B = 4.5 kG. We did not consider the track distortions introduced by magnetic field non uniformities, as we think that also this effect can be corrected knowing the field distribution.

VI.1 - Apparatus with Narrow Gap Spark Chambers. -

In the error evaluation we have assumed an apparatus described in details in[16] and schematically shown in Fig. 19a

a) - Errors Due to Coulomb Scattering. -

The multiple scattering effect was evaluated in the case of pions. The results are summarized in the following table:

p_π (GeV/c)	0.5	1.0	1.5
$\Delta p/p$	1.6%	1.6%	1.6%
$\Delta\delta$	0.6°	0.3°	0.3°
$\Delta\psi$	0.7°	0.4°	0.3°

where δ is the angle between the trajectory and the optical axis and ψ is the azimuthal angle.

These errors will be smaller in the case of wide gap spark chambers especially if the electrodes are of wire, because the material traversed by the particle will be much less.

b) - Errors Due to Spark Measurements and Fluctuations. -

The errors $\Delta p/p$, $\Delta\delta$, $\Delta\psi$ are expressed as functions of the standard error ΔS on the track sagitta projected on a plane perpendicular to the optical axis (for example tracks with $\delta = 90°$ give $\Delta p/p \simeq \Delta S/S$). For ΔS and $\Delta\psi$ we employ formulas usually used in fit-programs for bubble chamber and spark chamber events[13].

ΔS depends on σ_y (total error on each spark) and on the number of independent sparks measured. For example for the apparatus shown in Fig. 19a and sketched as following,

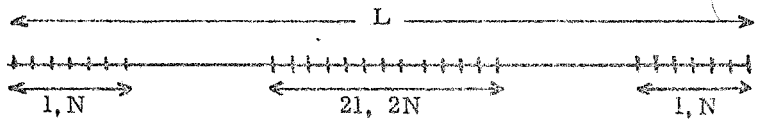

N (number of sparks) = 6 l = 6 cm L = 80 cm

we have:

$$\Delta S = \left(1 + \frac{2l}{L}\right) \frac{\sigma_y}{\sqrt{N}}$$

The resulting errors $\Delta p/p, \Delta\delta, \Delta\psi$ can be summarized in the following table:

p_π (GeV/c)	0.5	1.0	1.5
$\Delta p/p$	0.6%	1.2%	1.7%
$\Delta\delta$	.05°	.05°	.05°
$\Delta\psi$	.05°	.05°	.05°

c) Total Errors. -

The total errors resulting from the squared combination of the error above discussed are:

p_π (GeV/c)	0.5	1.0	1.5
$\Delta p/p$	1.8%	2.1%	2.5%
$\Delta\delta$	0.6°	0.3°	0.3°
$\Delta\psi$	0.7°	0.4°	0.3°

In Fig. 19c is shown the dependence of $\Delta p/p$ on p_π for two different δ values.

VI.2 - Apparatus with Wide Gap Spark Chamber. -

Such apparatus for trajectories with $\delta > 45°$ was described in § II, c) and its essential features are summarized in Fig. 19b. As some parameters of these spark chambers will be fixed by experimental measurements on prototypes we will not give the results of the calculations as for the previous apparatus but only discuss the main factors affecting the accuracies.

a) - Errors Due to Coulomb Scattering. -

In the case of the previous apparatus this error was determined by the scattering in the second spark chamber and by a smaller amount in the gas (air, helium or neon). The mean thickness of the 4 wide gap spark chambers interposed along a trajectory is determined by the wire diameter and by the spacing between wires. The wire thickness will be fixed by tests on prototypes; nevertheless assuming a 1÷2 mm spacing and a 100μ wire diameter, we get an unimportant contribution to the error. Moreover the δ and ψ angle measurement accuracy will be certainly greater as the Coulomb scattering is the main limiting effect.

b) - Errors Due to Spark Fluctuations. -

As the two arrangements have the same inner spark chamber, the accuracy in the first part of the trajectory will be the same. The remaining number of points in the two cases is the same but they will certainly be measured with a greater precision with the wide gap apparatus. As mentioned above (§ V) also the accuracy σ_y for spark localization will be measured on prototypes, so we do not report here an evaluation for this arrangement.

c) - Total Errors. -

The errors caused by the optics and the measuring device will probably dominate the overall accuracy. Assuming an error $\sigma_y^{tot} \simeq 150\mu$ for all these effects, we obtain at 1.5 GeV/c $\Delta p/p \simeq 1.3\%$.

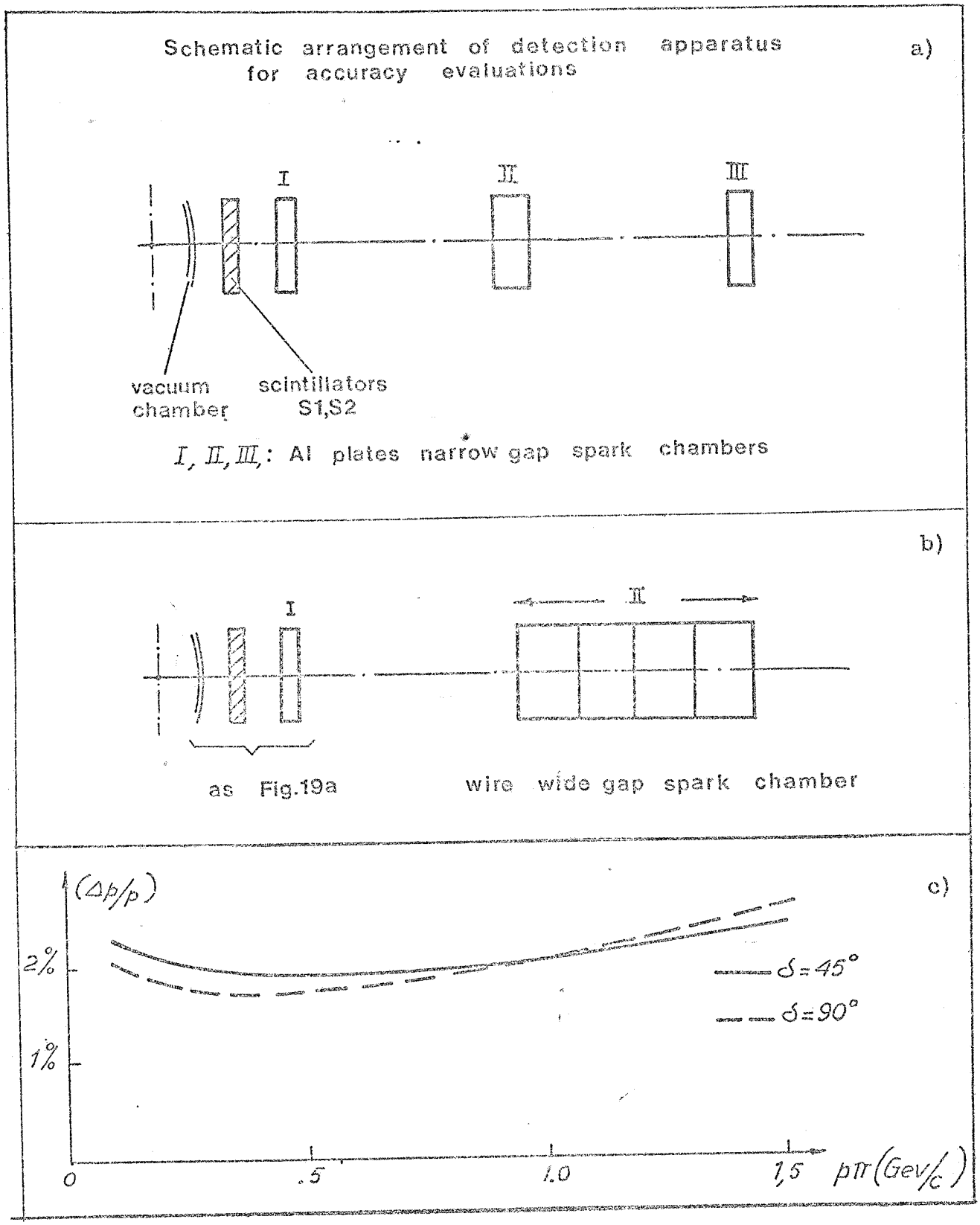

FIG. 19 - a) and b): schematic drawings of the two apparatus analysed in § VI; in a) the II chamber is assumed made with Al foils glued on polyurethane plates. - c) $\Delta p/p$ as a function of p for two δ values for the apparatus sketched in fig. 19a (with narrow gap spark chambers).

d) - Accuracies for Particles Trajectories with $\delta \leq 45^{\circ}$. -

Trajectories with $\delta \leq 45^{\circ}$ are detected with 2 plane electrodes wire bigap spark chambers (C 3) mounted perpendicularly to the magnet axis, each 20 cm thick and spaced by 20 cm (see § II, c) and Fig. 7). The value of the component $p_L = \vec{p} \times \vec{B}/|\vec{B}| = p\cos\delta$ is obtained by measuring the precession angle γ between these two spark chambers:

$$\gamma = \frac{3\,BL}{p\cos\delta} \times 10^{-4}\ \text{rad}, \qquad B\ (KG), \quad p\ (GeV/c), \quad L = 60\ \text{cm}, \quad \gamma = \varphi_1 - \varphi_2$$

In Fig. 20 is shown the dependence of γ on p. The track length l_v changes with δ taking values between $l_v = 3.5$ cm ($\delta = 10^{\circ}$) and $l_v = 16.8$ cm ($\delta = 40^{\circ}$). On the film this means .7 mm and 3.3 mm length for magnification I = 50. The γ error is given by:

$$\Delta\gamma \simeq \sqrt{24}\ \frac{\sigma_y}{l_v \sqrt{N}}$$

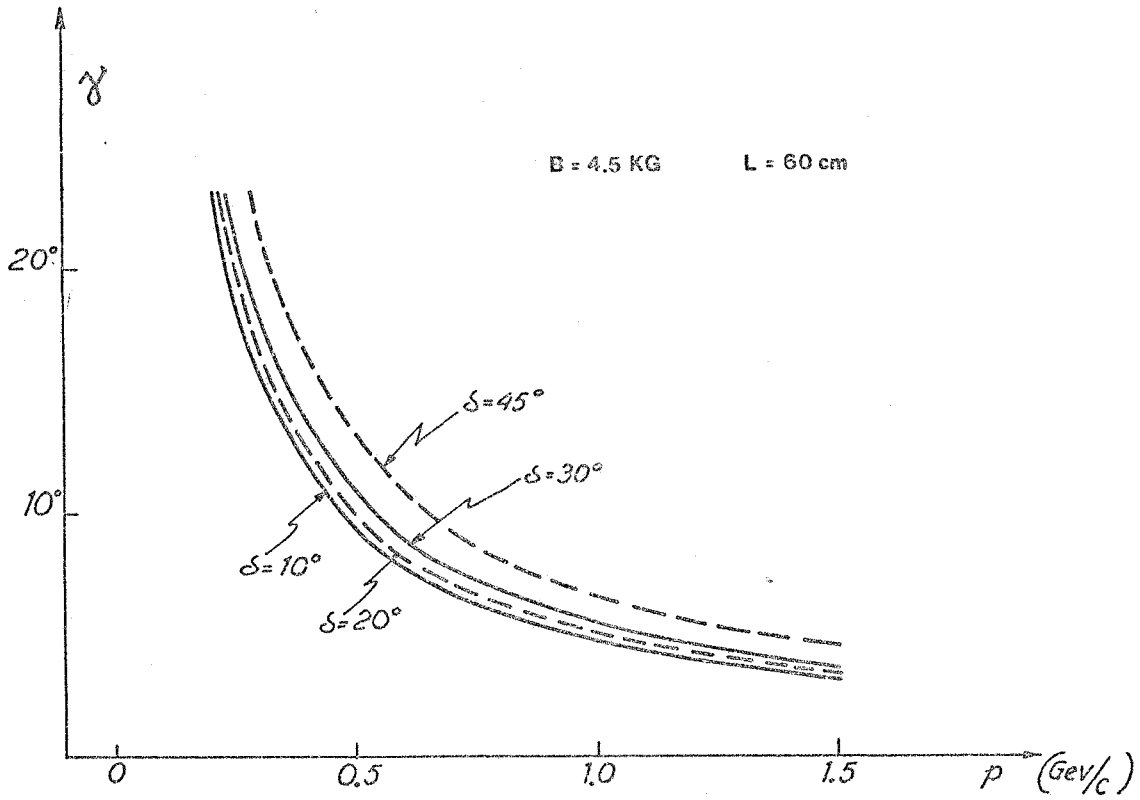

FIG. 20 - Precession angle γ of the momentum component perpendicular to B, between the 2 plane wire spark chambers C3, as a function of p for many δ values. L is the distance between the first and the second C3 chamber.

where N is the number of independent points measured in each track (N = 8 in our case). The minimum distance between two measured points on the film ($\delta = 10^{\circ}$) is 90μ. To make an estimate of the error on momentum we assume σ_y^{total} 150μ :

$$\frac{\Delta p}{p} = \sqrt{\left(\frac{\Delta p_L}{p_L}\right)^2 + \left(\text{tg}\,\delta\,\Delta\delta\right)^2} \simeq \frac{\Delta\gamma}{\gamma}$$

The results can be summarized in the following table:

δ \ p_π (GeV/c)	.5	1.0	1.5
10°	4.5%	8.7%	13.5%
30°	1.2%	2.3%	3.5%

The errors introduced by the coulomb scattering are negligible as the amount of traversed material is very small.

VII. - MASS RESOLUTION. -

By means of a Montecarlo calculation[17] the following reactions have been studied:

$$e^+ e^- \rightarrow \pi^+ \pi^- \pi^0 \qquad\qquad e^+ e^- \rightarrow \pi^+ \pi^+ \pi^- \pi^-$$

The previously discussed accuracies of the apparatus were used to calculate the resolutions. The evaluations were made both with the solenoid in the transverse and in the longitudinal configuration. In the transverse configuration the magnetic field of the solenoid was taken as 4.5 kG or the maximum value compatible (see § III) with Adone (without correction for the lens effect) whichever was smaller.

For the first reaction[18] in Fig. 21 is shown, as a function of the total energy, the value of the squared missing mass plus and minus its standard error ($m^2_{\pi^0} + \Delta MM^2$, $m^2_{\pi^0} - \Delta MM^2$). For the second reaction we give in Fig. 22 missing mass distributions for two different energies in the transverse configuration. It can be seen that when all reaction products are detected, the quantity ΔMM^2 has a pronounced asymmetry.

VIII. - USE OF EXTERNAL CHAMBERS. -

a) - Photon Detection. -

The photons can be converted in the aluminium main coil (0.8 RL) or in the iron converters interposed between the external bigaps. We have studied the photon detection efficiency $\mathcal{E}(E_\gamma, s)$ defined as the ratio between the number of photons "seen" by the spark chambers and the number of incident photons. E_γ is the photon energy and s is the thickness of each converter of the system shown in Fig. 6.

The efficiencies were extracted using experimental data obtained with a simple counter system[19] simulating spark chambers. Nearly monochromatic photons produced in a thin radiator by positrons from the Frascati pair spectrometer, were incident on an arrangement of counters and variable absorbers. Assuming that a scintillator reacts the same as a spark chamber to a low intensity shower, the measured efficiency of the counters should be equivalent to that of a spark chamber system. The resultant efficiencies, assumed accurate to ~5%, are shown in Fig. 23 for different thicknesses of iron or lead absorber, preceded by .8RL of aluminium to simulate the coil, and for three different criteria of detection, i.e. that the incident photon be detected through its shower products in at least 1, 2, or 3 chambers (bigaps).

As can be easily seen it is useful to use lead as converter in order to achieve a better detection efficiency for low energy photons. Moreover for the same reason it is advisable to keep the thickness of each converter small (~ 1/3 RL). If mechanically possible we shall use lead as absorber in the external arrangement, otherwise iron or a sandwich of iron+lead in which the iron acts as support for the lead. In the solution shown in Fig. 6 the total thickness in RL units of the main coil and of all the external absorbers is ≃5. Finally were have estimated as ~1.5° the angular accuracy in photon direction which can be obtained from shower analysis.

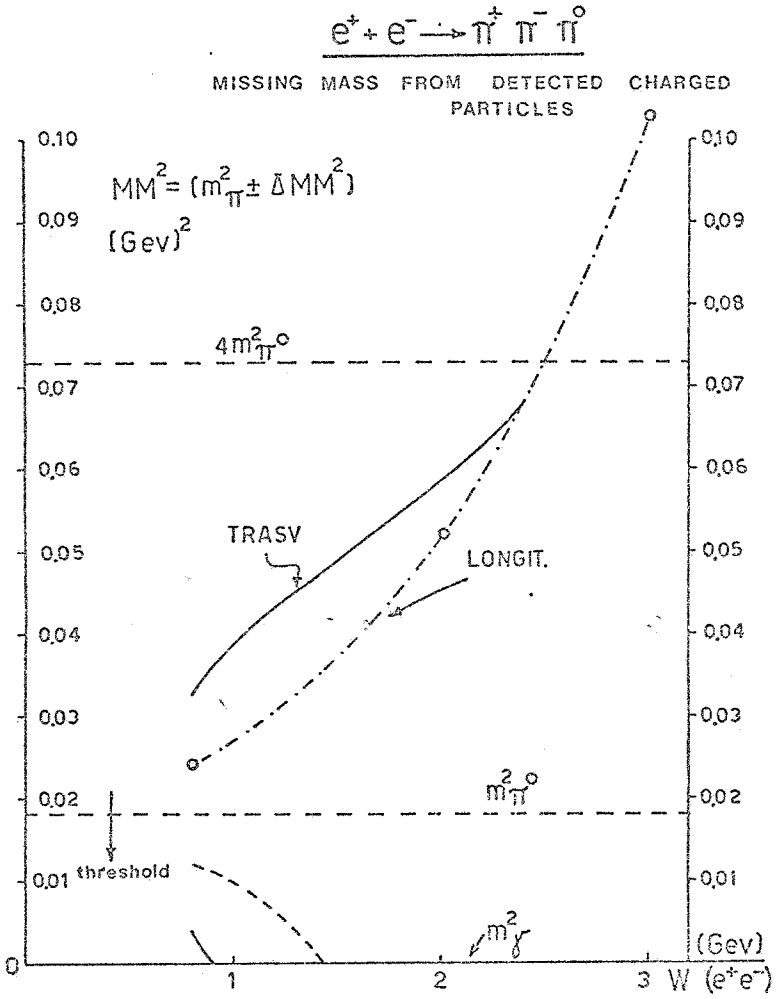

FIG. 21 - Squared missing mass $m^2_{\pi o}$ from the charged products, plus and minus the standard error ΔMM^2 as function of the total energy of the beams for the apparatus in the transverse and longitudinal arrangement. Below 2.4 GeV the calculations for the transverse arrangement assumed a smaller magnetic field value which would not interfere with ADONE if no corrections were applied.

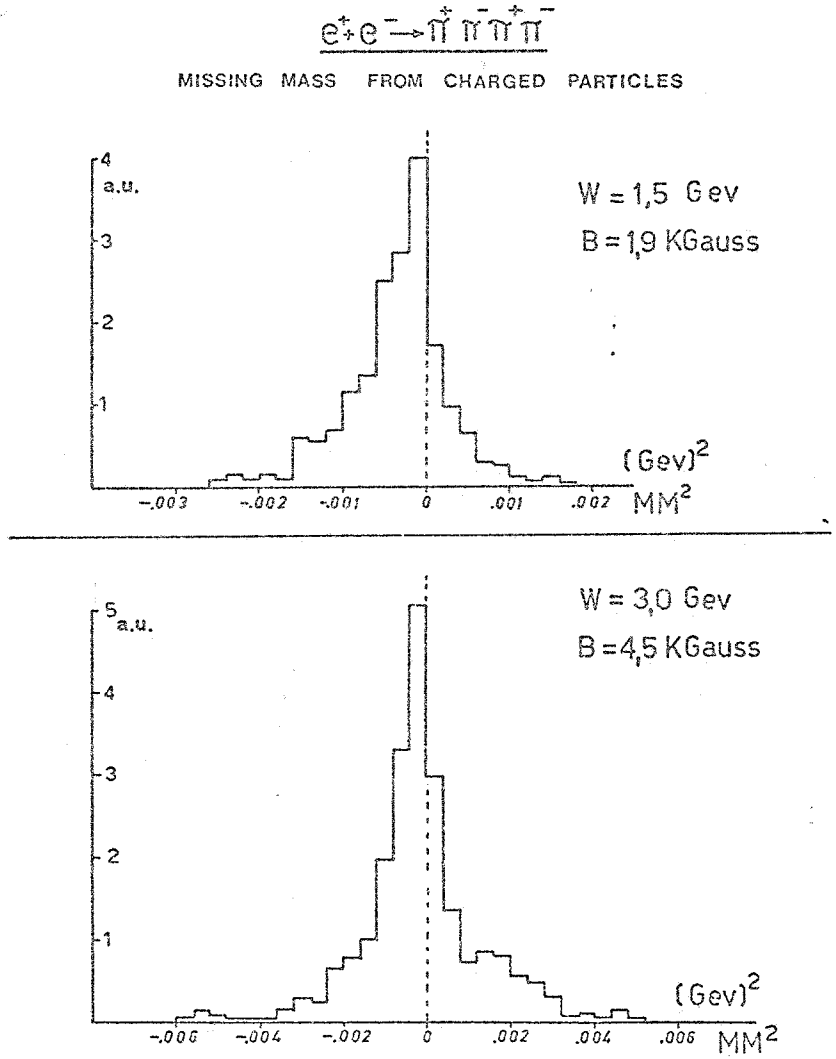

FIG. 22 - Squared missing mass distribution at energy values W = 1.5 GeV and 3.0 GeV.

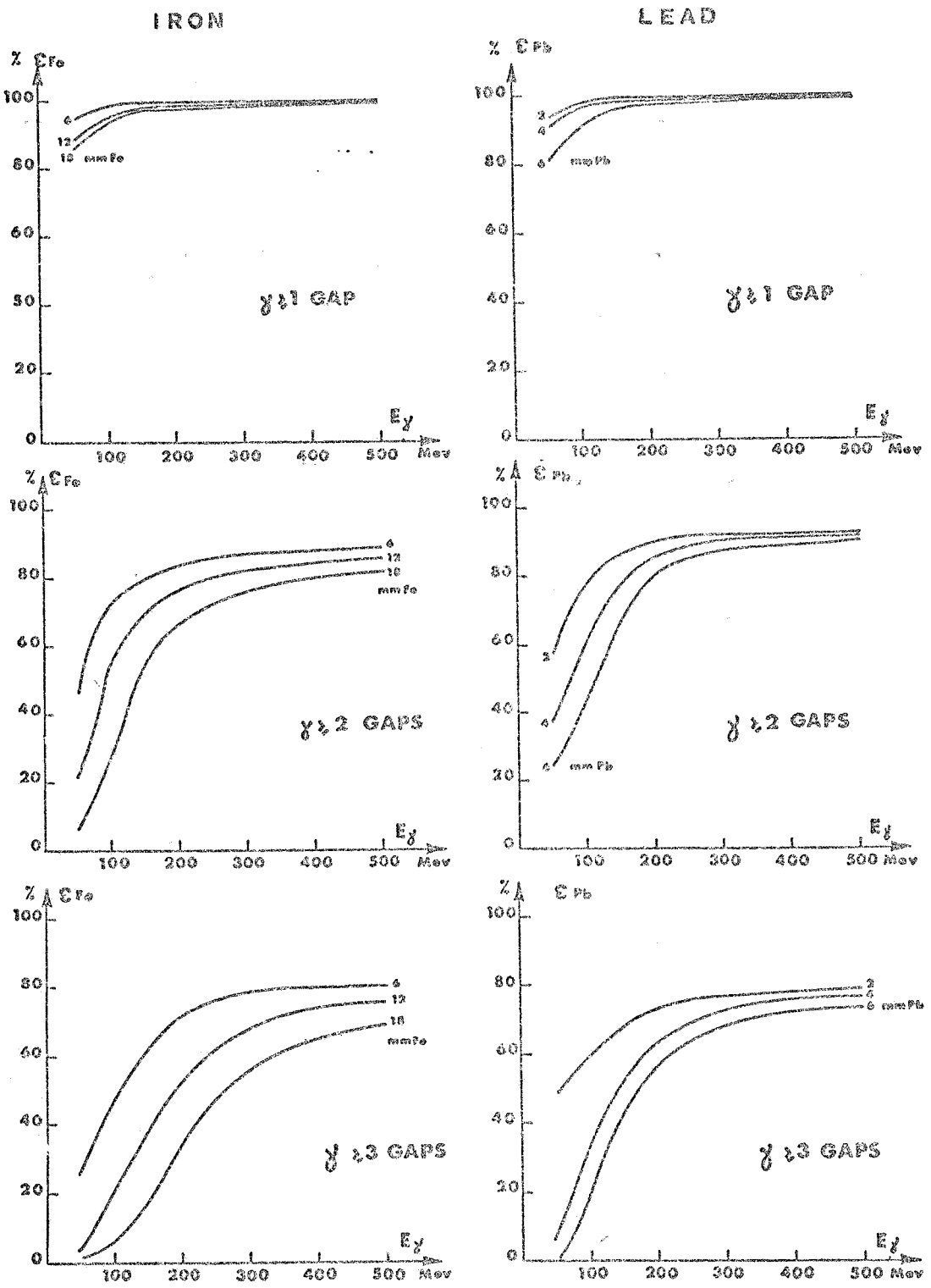

FIG. 23 - Detection efficiency for photons $\varepsilon(E_\gamma, s)$ as a function of E_γ for several thickness s of lead and iron.

b) - Discrimination Between Electrons and other Charged Particles. -

It is possible to recognize the electrons by their showers produced in the external chambers. The behaviour of an electron shower in a matrix of absorber and spark chambers has been extensively studied[20]. Assuming that these results are applicable to our system, the mean spark multiplicity for electrons with $E \leq 800$ MeV has a maximum at $\simeq 3$ RL and extrapolating to $E = 1.5$ GeV the maximum is at $\simeq 4$ RL, the value choosen for our external spark chamber system.

c) - π-μ Discrimination. -

We can discriminate π fro μ on the basis of nuclear interaction. For this reason the total thickness of iron in the external chambers has been increased to $\sim 1\ \lambda_c$ (collision length). The following table gives the percentages of single π or π -pairs that do NOT interact in the system shown in Fig. 6:

	single π	pair π
Aluminium coil	78%	61%
Aluminium coil and iron in ESC system	37%	11%

IX. - LUMINOSITY MEASUREMENTS. -

For luminosity measurement up to now 3 different methods have been proposed. We summarize their features in the following.

1) γ detection tangent to the beams at the interaction point;
2) elastic e^+e^- scattering at small angles;
3) elastic e^+e^- scattering in the angular interval accepted by the experimental apparatus.

The first method which was studied in detail by Tazzari[21] is based on the application of the single and double bremsstrahlung ($e^+e^- \rightarrow e^+e^-\gamma$, $e^+e^- \rightarrow e^+e^-\gamma\gamma$) and annihilation ($e^+e^- \rightarrow \gamma\gamma$) reactions.

The difficulty in measuring the single bremsstrahlung process is caused by bremsstrahlung on the residual gas, which in the standard working conditions of Adone, is comparable to the former. For this reason an independent measurement is required for gas bremsstrahlung background subtraction. We expect[21] however the signal to noise ratio will be such as to yield a luminosity measurement accurate to $\simeq 10\%$. The presence of the gas bremsstrahlung background makes the first method more a control of the working conditions and stability of the storage ring than a true luminosity monitor. Each Adone straight section is supplied with two thin windows for the γ detection at 0° and 180° which can be made with two glass-lead Cerenkov counters. For this reason there is no difficulty in using the first method with the magnet.

The second method will be used in Adone as monitor by Conversi et al. who will study the process $e^+e^- \rightarrow \mu^+\mu^-$. This group[22] expects that the apparatus they have built to detect the elastic scattering events at small angles (between 3.5° and 6.0°) will give a luminosity measurement accurate to 1%. This device, consisting of two counters telescopes, is useful only if the vertical displacement of the interaction point is kept within about 2 mm. The installation of such a device in our apparatus is possible but will require the construction of a vacuum chamber with particular shape and will complicate the construction of the main coil to accomodate the new vacuum pipe. Furthermore the partial compensation of the transverse magnetic field has the effect of displacing the interaction point from 1 cm to 5 cm, depending on the energy. For this reason the two telescopes must be provided with an energy variable alignment as otherwise the monitor response would be energy dependent.

The third method uses the elastic scattering events gathered by the experimental apparatus during the measurement. To obtain the luminosity we need to know the elastic scattering cross section which, at least at low energy ($E \ll 500$ MeV), can be calculated with quantum electrodynamics. For higher energies the validity of quantum electrodynamics must be confirmed with an independent measurement which can be obtained from the first generation Adone experiments. The counting rate for elastic scattering will be about 300 per hour. As the expected

counting rate for the processes that will be studied with the apparatus is of the order of a few per hour, the statistical error in this monitor is negligible. This kind of normalization has the advantage of being performed with the same apparatus and not with an independent device, but has the disadvantage of requiring full film analysis.

The need of an instantaneous luminosity monitor, even if a rough one, requires that the magnet be furnished with a monitor of the first or the second type. The choice will depend on the experience acquired in the first working period of Adone. The simplest solution consists of the use of monitor 1) to control the machine working conditions and to obtain a first rough estimation of the luminosity, and of monitor 3) for final normalization. The comparative study of methods 1) and 2), which is scheduled at Adone, will ascertain if the first method can be employed and will obtain the calibration between the monitors 1) and 2).

X. - GAS CONTROL SYSTEM. -

The 2 main functions of any spark chamber gas control system are (see Fig. 24):

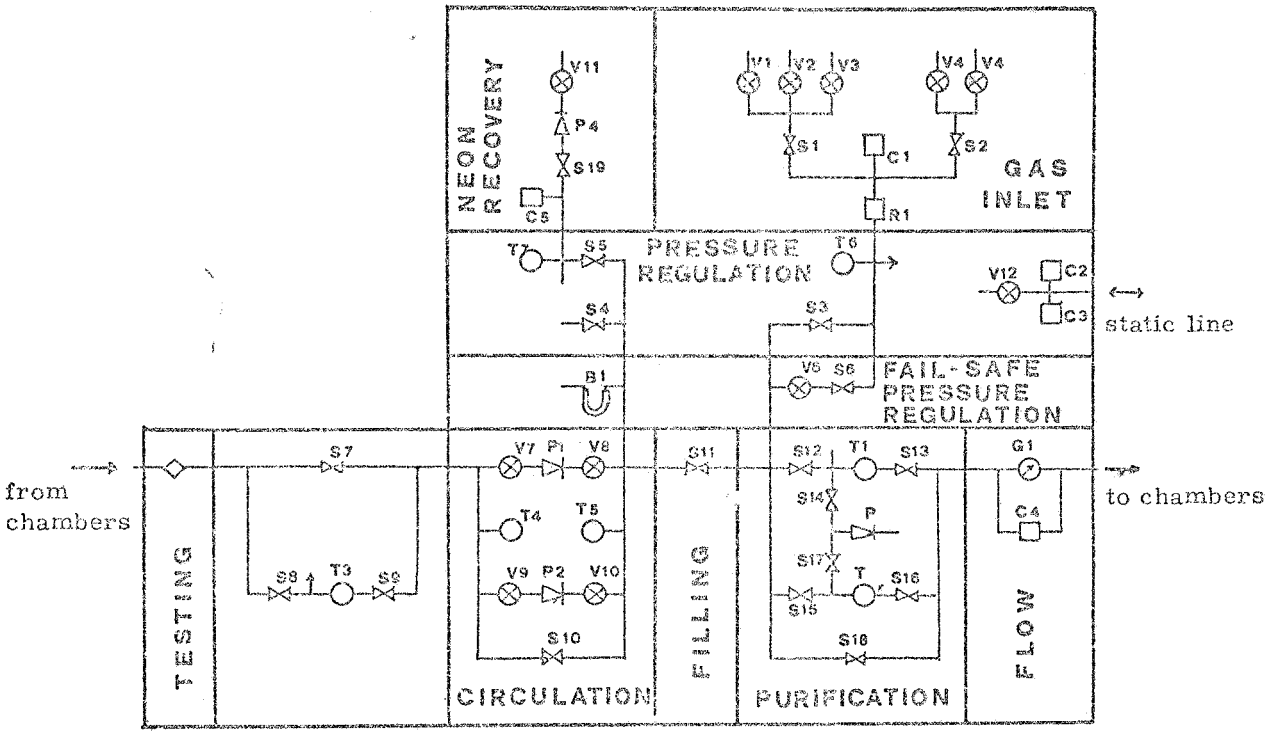

FIG. 24 - Schematic drawing of the gas control system

1) - Purification - The gas is continuously circulated through a LN_2 cooled trap.

2) - Pressure regulation - Compensation is made for leaks or for changes in ambient temperature, or pressure. Pressure is kept 1-3 cm of H_2O above atmospheric pressure.

For use at Adone there are 2 additional features which are highly desirable. These are:

3) - Remote control - The control panel should not be situated on the experimental floor which is high radiation area. Remote operation of the gas system would not require frequent shut-down of Adone.

4) - Safety - The system should be fool-proof with respect to implosions or explosions of spark chambers. In addition the system should be as foolproof as possible regarding human error leading to an expensive loss of large quantities of neon, and it should be foolproof if power fails.

For the gas control system for the magnetic detector there are several more considerations which become important. These are:

5) - Minimizing neon wastage - The design of the magnetic detector has not been completely fixed yet, but the volume of neon required will be either 2000 liters or 6000 liters, depending on whether the spark chambers only or the entire magnet is filled with neon. It is reasonable therefore to plan a gas system for 4000 liters of neon. This much neon will cost approximately $ 500. It is therefore good economy to spend several times this amount on the gas control system itself in order to have a system which conserves neon. In particular, the gas system should allow an economical procedure for the initial filling of the spark chambers and it should provide a means to recover the neon when it is necessary to open the spark chambers to the air.

6) - Filling procedure - It may be presumed that it will not be feasible to pump the spark chambers down to vacuum before filling. The least expensive filling procedure we are aware of is to flush the chambers with 7 volumes of CO_2 gas. This leaves only about 0.1% air. Then neon may be added while the CO_2 is frozen out be a cold trap. Such a procedure has been successfully used by Keller, Schluter and White at Argonne.

7) - Recovery procedure - The neon may be recompressed and stored. For this purpose it is displaced by CO_2 again. Whatever CO_2 exits from the chamber is frozen out by a cold trap, so that it is not recompressed with the neon.

8) - High circulation speed - The filling procedure above will require the circulation of 14 volumes of gas before the neon reaches 99.8% purity. If 2 days are allowed for filling, then the pumping speed must be 1200 liter/hour. Liquid nitrogen has a heat of vaporization of 50 cal/g and a density of 800 g/liter. Neon has a density of 1 g/liter and a specific heat of 1/4 cal/°C. The neon drops about 200°C. Therefore we require 1.3 liters of LN_2 per 1000 liters of neon purified. Including LN_2 wasted in initial cooldown and in boil-off, a 50 liter supply dewar would last 24 hours before needing to be refilled. This LN_2 would be led automatically to the dewar containing the cold trap.

9) - Redundancy - The system should be designed so that 2 cold traps may be alternated with one being baked out while the other is in use. Also, there should be a backup circulating pump in case the regular circulating pump fails.

Considerations 1) through 9) have gone into the design of the gas control system presented in this report (see Fig. 24).

ACKNOWLEDGEMENTS. -

During this work we received much help from numerous groups of the "Laboratori Nazionali di Frascati", for which we are indeed grateful.

In particular we are deeply indebted to Prof. R. Querzoli for his continuous encouragement and interest. We are happy to thank Prof. F. Amman for the attention devoted to the problem of magnet-beam interactions, for many useful suggestions and for securing the assistence of the machine group.

It is a pleasure to thank Dr. A. Tenore who performed calculations on magnet-beam interactions, Mr. A. Catitti for his constant collaboration, Mr. G. DiStefano and G. Bonini who helped us in the spark chamber design, Dr. A. Cattoni, Prof. C. Pellegrini, Prof. F. Scaramuzzi for many useful discussions and Mr. S. Stipcich for the publishing of this and previous reports.

BIBLIOGRAPHY AND REMARKS. -

(1) - U. Amaldi et al., LNF-67/3 (1967).
(2) - The magnet has been designed in detail by the LNF Magnet Group. This group is now studying the field map of the entire magnet system.
(3) - G. P. Murtas, Cylindrical Spark Chamber with Light Reflecting Electrodes, Nuclear Instr. and Meth. 62, 298 (1968).
(4) - This point is discussed in[16] in which the authors study the spark jitter effects in a polygonal system of plane spark chambers and conclude that the lateral jitter in a plane perpendicular to B makes the accuracy in momentum measurement too low. This effect does not exist in a cylindrical system in which all the trajectories coming from the interaction point make very small angles with the electric field.
(5) - Chambers of this kind have been built in other laboratories and do not seem to present any particular difficulty.
(6) - The maximum thickness of material acceptable in the intermediate part of the trajectory for a system such as the one analyzed here was defined in[16] and is about 250 μ. Obviously, greater thickness can be accepted at the beginning or at the end of the analyzed curve so that, for example, plate thickness in the first chamber is not particularly critical.
(7) - Roberts et al., IEE Nuclear Trans., p. 121 (1965).
(8) - The front walls of the internal wire spark chambers are in reality transparent. Nevertheless the high precision measurements required for track position (§ V) imposes a very severe optical requirement on these walls in the case that the image has to pass through them. This complication was thought excessive.
(9) - L. Paoluzzi and R. Visentin, Nuclear Instr. and Meth. 65, 345 (1968).
(10) - E. Schiavuta, Memorandum interno Adone ME-11.
(11) - In this evaluation the dimensions of spark chamber frames (not shown for simplicity in figures) were taken into account.
(12) - For a more complete discussion on § V, VI, VII see[16]. For a deeper discussion on the possibilities of distinguishing the reactions $e^+e^- \to \pi^+\pi^-$, $\pi^+\pi^-\pi^0$, $\pi^+\pi^-\pi^0\pi^0$ see "Relazione Gruppo Magnete Adone" (April 1968).
(13) - P. Asbury et al., Nuclear Instr. and Meth. 46, 61 (1967).
(14) - J. P. Garrou, D. Grossman and K. Strauch, Rev. Sci. Instr. 36, 264 (1965).
(15) - J. H. Christenson, A. R. Clark and J. W. Cronin, IEE Trans. on Nuclear Sci. NS 11, 310 (1964).
(16) - M. Nigro and R. Santangelo, Memorandum Interno Adone ME-18.
(17) - The programming work was performed by M. Locci and M. A. Spano-Mencuccini of the S. C. N. of Frascati.
(18) - The detection efficiency for two charged π in the reaction $e^+e^- \to \pi^+\pi^-\pi^0$ was calculated considering the dynamics of the process for that part of the apparatus with $\vartheta \geq 45^\circ$. The total efficiency value of $\eta \simeq 0.4$ is energy independent in the range $W(e^+e^-) = 1 \div 3$ GeV.
(19) - G. Capon and G. P. Murtas, to be published, and G. P. Murtas and D. Scannicchio, Memorandum Interno Adone ME-19.
(20) - Augustin et al., Nuclear Instr. and Meth. 36, 213 (1965).
(21) - S. Tazzari, Memorandum Interno Progetto Adone E1.
(22) - G. Barbiellini et al., Proposta di esperienza con l'anello di accumulazione "Adone" di Frascati, Università di Roma, Nota Interna 89 (1965).
(23) - D. Grossmann and J. Matthiae, Memorandum Interno Adone ME-12.
(24) - W. Ash, Memorandum Interno Adone ME-22.
(25) - W. Ash and D. Bisello, Memorandum Interno Adone ME-21.
(26) - The drawings in Fig. 4 have been kindly furnished by A. Catitti and G. Pasotti from the report LNF-68/72 (1968).

APPENDIX - LONGITUDINAL MAGNET. -

The longitudinal magnet - detection apparatus is illustrated in Figs. 25, 26, 27, 28, 29. Those parts that are substantially different from the corresponding items of the transverse design will be discussed here.

a) - Detection Apparatus. -

Three layers of cylindrical spark chambers are introduced into the solenoid as shown in Fig. 25. The chamber closest to the beam, C_1, is of 6 gaps, 5 mm each. The second and third chambers may be either wide gap or narrow gap, whichever is more suitable (see discussion in § II, V). The external spark chambers and trigger system are the same as in the transverse case.

b) - Compensation. -

As the magnetic field lies along the beam direction there is no first order effect on the Adone beams as distinct from the transverse case. Compensation therefore is necessary only to reduce second order effects, e.g. coupling of vertical and radial betatron oscillations, and can be much more simply done in this case.

c) - Flux Return. -

Due to the proximity of the quadrupoles to the ends of the solenoid, it is essential to reduce to a minimum the stray flux. At each end of the solenoid is placed a large 15 cm thick iron plate for flux return. To accomodate the optical view of the chambers, windows are cut in these plates in correspondence to the location of the internal chambers (see Fig. 26). The iron of the external chambers completes the flux path.

d) - Support. -

Since this magnet could not easily be made separable in a plane parallel to the axis, it is a fixed structure and once in place can only be moved transversally a distance equal to its radius to allow access. Hence a rather complicated disassembly sequence, requiring movable internal spark chambers and dismountably external chambers results as illustrated in Fig. 27.

f) - Optics. -

The optics[16, 23] consists of:

- two vertical external high precision mirrors, which send the two halves (right, left) of the internal spark chamber views to two separate cameras. The bottom of the quadrupole support must be modified to allow placement of the mirrors (see Fig. 28, 29);
- a complex of mirrors, inside the magnet, to direct the view of the small chambers (C_1) around the shadow of the quadrupole;
- a second set of internal mirrors behind the spark chambers inclined so as to provide a depth measurement;
- a conventional mirror system for the external chambers.

CONCLUSIONS. -

The solid angle considerations follow the same lines as those of the transverse case. Particles can be momentum analysed to high precision ($\sim 2\%$) in a solid angle of $.55 \times 4\pi$ str.; a less precise measurement ($\lesssim 10\%$) of momentum can be made on an additional $.15 \times 4\pi$ str.; finally a measurement of only direction can be made over an additional $.17 \times 4\pi$ str. (total solid angle $.87 \times 4\pi$ str.).

The external chamber system has a solid angle of $.56 \times 4\pi$ str.

This design presents such great mechanical and optical complications that it would be feasible to use this arrangement only in the event that the transverse magnet produces completely unexpected and unmanageable interferences with Adone beams.

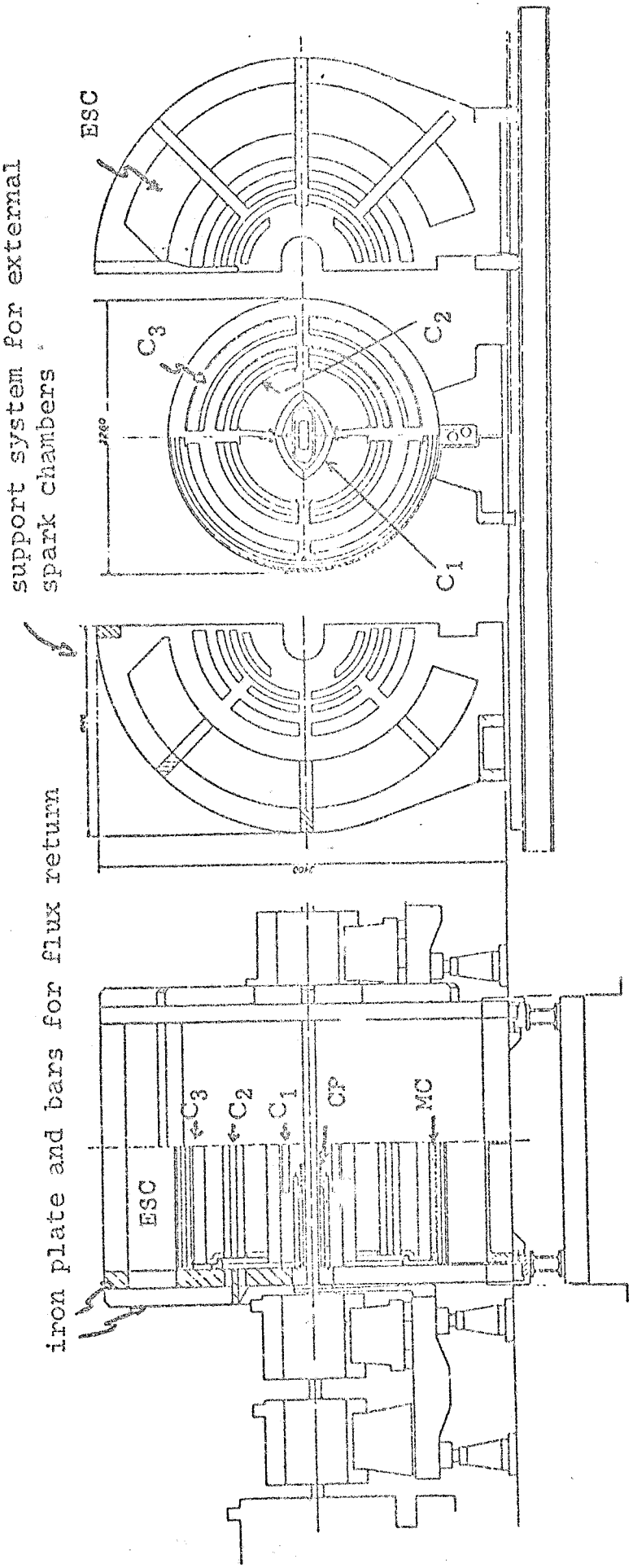

FIG. 25 - Sectioned views of the longitudinal arrangement: MC = main coil; CP = compensators; C_1, C_2, C_3 = internal spark chambers; ESC = external spark chambers.

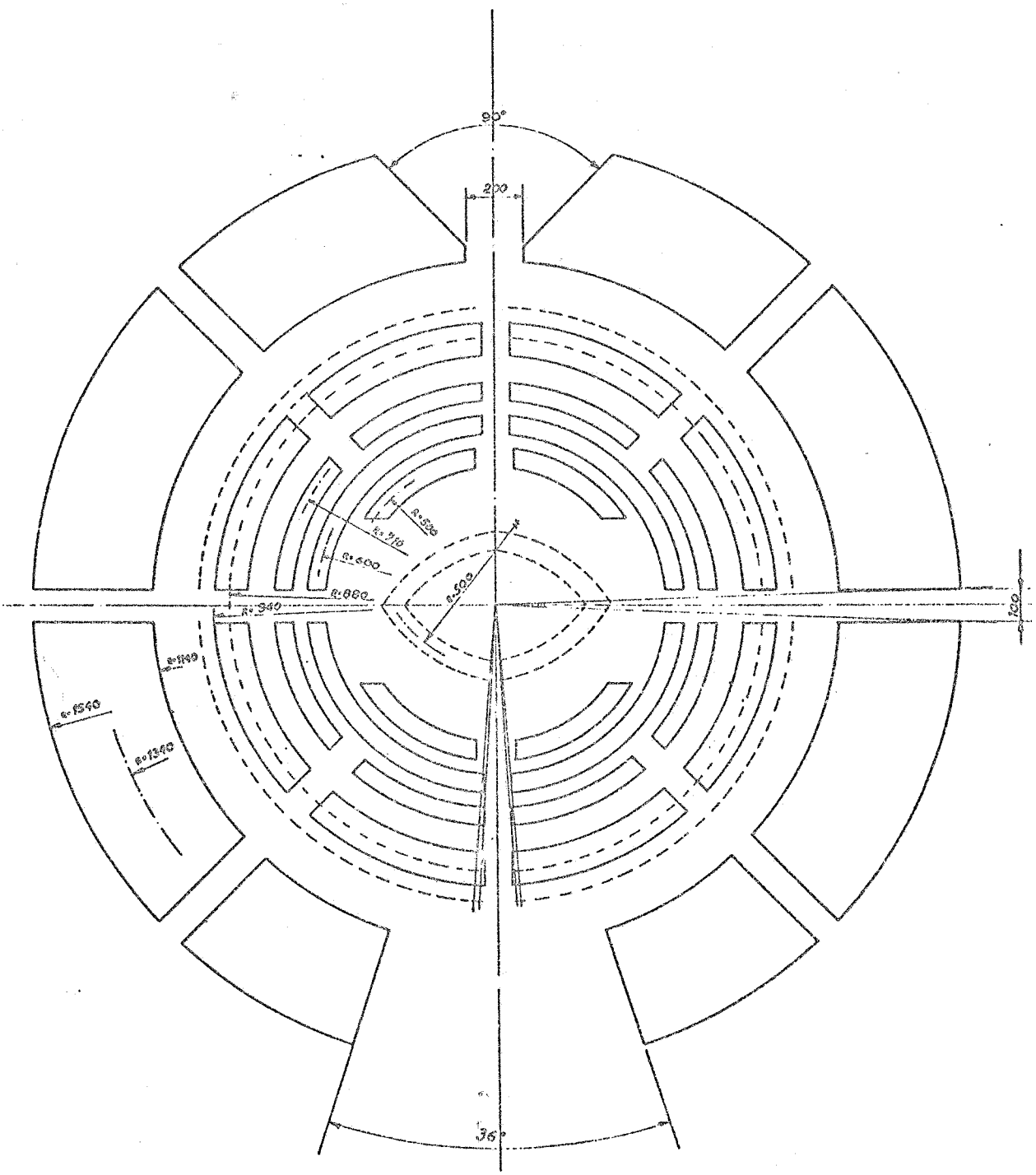

FIG. 26 - Front view of the spark chambers in the longitudinal arrangement. Only those parts of spark chambers observable through the apertures in the iron plate are shown.

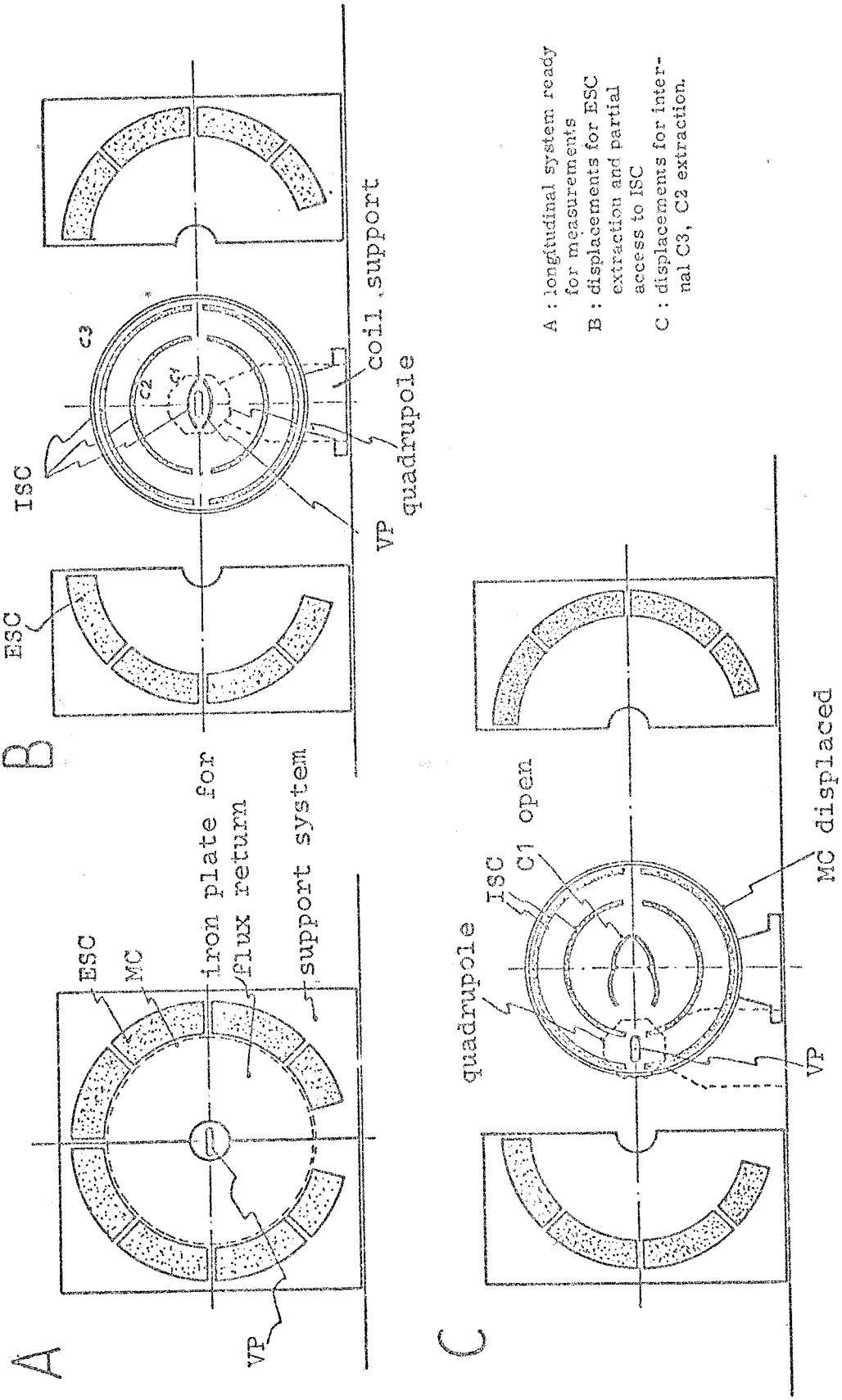

FIG. 27 - Disassembly sequence of the longitudinal magnet system : ISC = internal spark chambers (C1, C2, C3); ESC = external spark chambers; VP = vacuum pipe; MC = main coil.

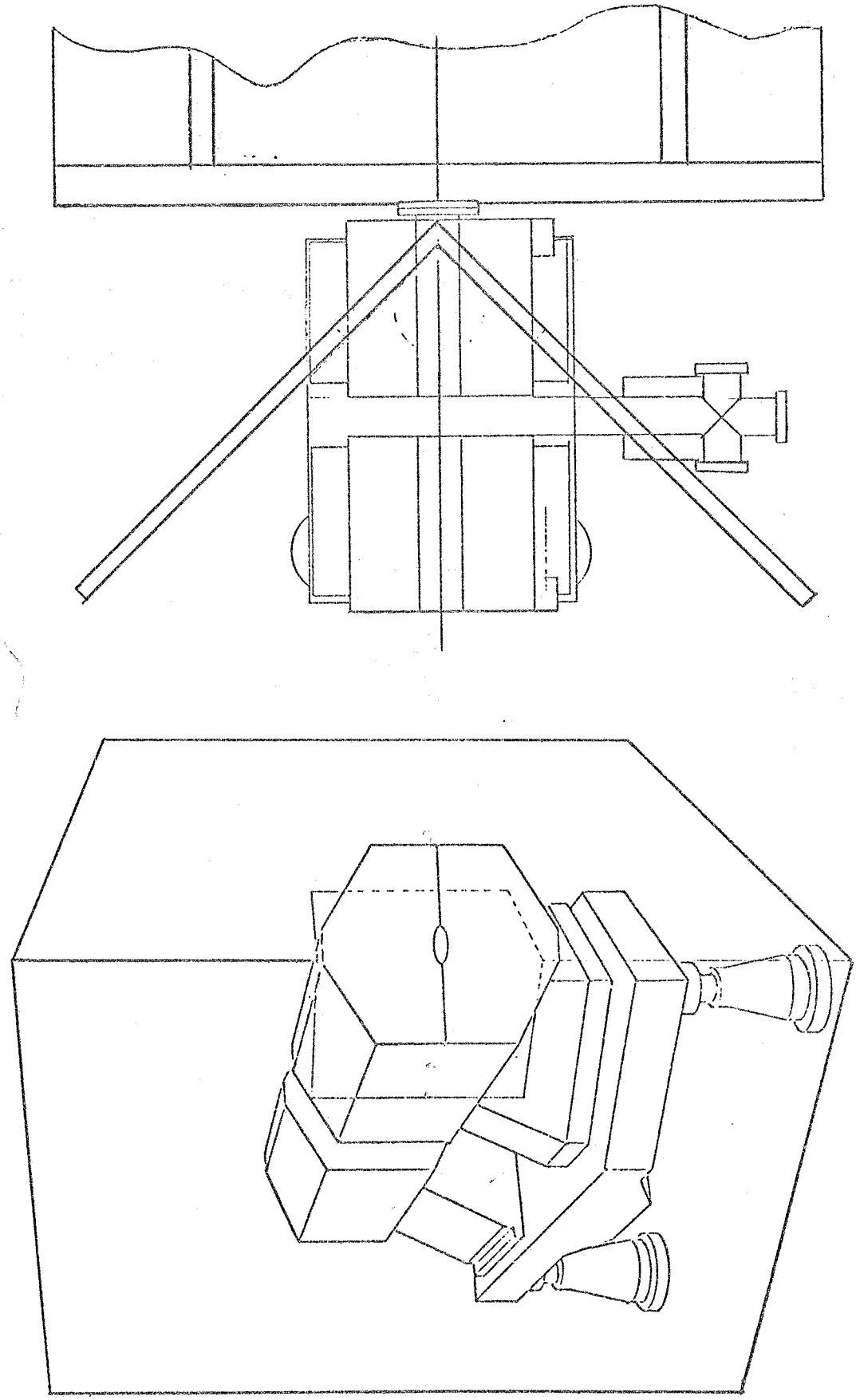

FIG. 28 - Front vertical mirrors.

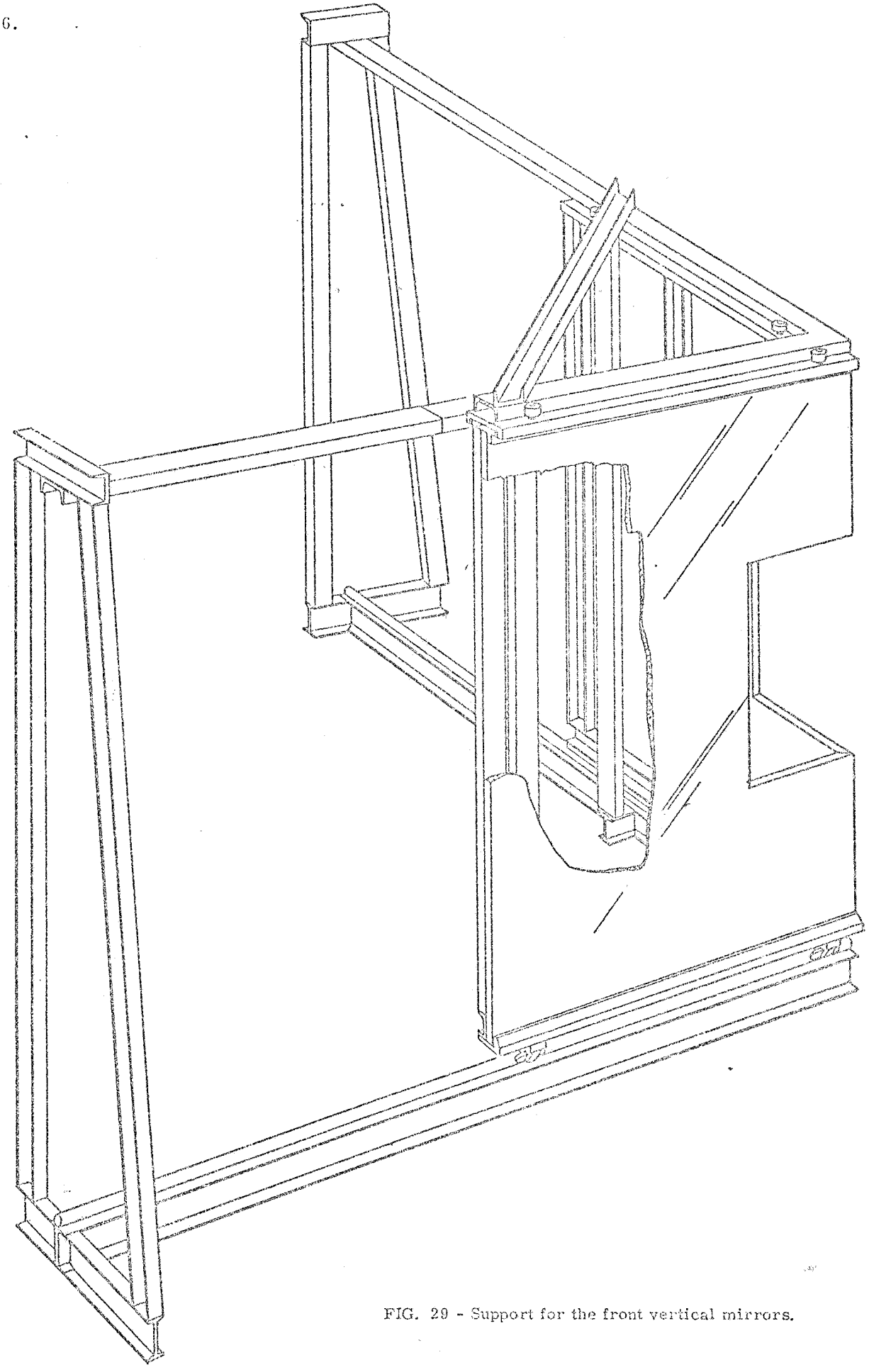

FIG. 29 - Support for the front vertical mirrors.